This is a preprint, the final version is subject to change, of the American Mineralogist (MSA)
Cite as Authors (Year) Title. American Mineralogist, in press.
(DOI will not work until issue is live.) DOI: http://dx.doi.org/10.2138/am-2016-5651

Revision 1

Origin and Petrogenetic Implications of Anomalous Olivine From a Cascade Forearc Basalt

M.C. Rowe[1]*, F. J. Tepley III[2]

[1]SCHOOL OF ENVIRONMENT, UNIVERSITY OF AUCKLAND, AUCKLAND 1142, NEW ZEALAND
[2]COLLEGE OF EARTH, OCEAN AND ATMOSPHERIC SCIENCES, OREGON STATE UNIVERSITY, CORVALLIS, OR, 97331, U.S.A.

*Corresponding Author: Michael C. Rowe; Phone: +64 9 373 7599 x86682; Email: michael-rowe@auckland.ac.nz

Key Words: reaction pyroxenite, shoshonite, subduction, trace element, diffusion, mixing

Running Title: Subduction processes from anomalous olivine compositions

This is a preprint, the final version is subject to change, of the American Mineralogist (MSA)
Cite as Authors (Year) Title. American Mineralogist, in press.
(DOI will not work until issue is live.) DOI: http://dx.doi.org/10.2138/am-2016-5651

ABSTRACT

Erupted absarokitic-shoshonitic volcanics in subduction zones make up a relatively small proportion of the total erupted volcanic material. However, they are a critical component for quantifying subduction metasomatism and mantle source heterogeneity. This study examines the geochemistry of anomalous olivine within a forearc absarokite lava and associated tephra, a compositional end-member of the Cascadia subduction zone magmatism, to infer mantle heterogeneity and magma petrogenesis. Ni concentrations from the young (42 ka) Quartzville absarokitic basalt lava flow and tephra in the Cascade forearc are up to ~6400 ppm Ni with correspondingly low Ca, averaging ~850 ppm Ca in Fo_{91} olivine cores. Decreasing of Ni and Ca toward the olivine rims cannot be accounted for by simple fractional crystallization and instead necessitates magma mixing ± diffusive re-equilibration between the high-Ni, low-Ca olivine cores and low-Ni, high-Ca rims. $\delta^{18}O$ of olivine phenocrysts (5.64 ‰) are elevated compared to other Cascade compositional components and outside of range typically associated with peridotitic olivine, or olivine crystallizing from peridotite-derived basaltic magmas. Trace element contents of whole rock, melt inclusions, and scoria glass have high Sr, high Dy/Yb and low Y, characteristic of adakitic slab melts, however major element compositions are of an alkali-rich basalt. In addition, similar trace element compositions between all analyzed glasses, indicates a related petrogenesis between all components. We propose that a slab partial melt has reacted with depleted harzburgite in the mantle wedge, underlying the older Western Cascades (~40-10 Ma). Reaction of the siliceous slab-derived melt with depleted harzburgite could produce a metasomatized, zoned pyroxenite-harzburgite mantle source. High-Ni, low-Ca olivine crystallize from melts of the subarc mantle reaction-pyroxenite. Later melting of the metasomatized harzburgite produces the absarokitic bulk composition, with olivine compositions

recording diffusive re-equilibration following incorporation of pyroxenite-derived olivine in a peridotitic magma. Importantly, then, the observed olivine chemistry reflects mineralogical variations in the subarc mantle while melt trace element variations record melts/fluids derived from the subducting plate. High-Fo olivine rims (up to ~Fo_{94}) appear to be the result of late stage oxidation in the lava flow resulting from SO_2 degassing and are unrelated to the otherwise complex magma petrogenesis.

INTRODUCTION

Shoshonitic magmas, including the more primitive absarokites, are found in volcanic arcs around the world, typically associated with low degree partial melts of highly fluid-metasomatized mantle (e.g., Kamenetsky et al., 1995; Luhr, 1997; Hesse and Gove, 2003; Rowe et al., 2009). Given their normally small erupted volumes, and formation as low degree partial melts, shoshonites may preserve evidence of small-scale heterogeneity lost during homogenization of larger melt fractions. In the Cascade volcanic arc, a global endmember for "hot" subduction (Syracuse et al., 2010), absarokites and shoshonites are rare. However, shoshonitic magmas comprise one of a number of distinct magmatic compositions, each providing insight into subduction zone magma genesis in the Cascadia system (Borg et al., 1997; Conrey et al., 1997; Reiners et al., 2000; Leeman et al., 2005; Schmidt et al., 2008; Rowe et al., 2009; Schmidt et al., 2013). This study focuses on the petrogenesis of the most primitive absarokite identified to date in the Cascade arc. In particular, prior research has identified the presence of anomalous olivine compositions, characterized by high Ni (>6000 ppm Ni) and low Ca (< 900 ppm Ca) contents in olivine ranging from ~Fo_{88-94} (Conrey et al., 1997; Rowe et al., 2006; 2009). Prior petrogenic models have not taken into account the significance of these

anomalous olivine grains. Here we utilize the unique mineral chemistry to create a holistic petrogenic model related to subduction zone processes in this global endmember of "hot" subduction.

SAMPLES AND ANALYTICAL METHODS

Samples

The herein named Quartzville basalt is located in the Quartzville mining district in the western forearc margin of the Oregon Cascades (Lat. 44° 36.047'N, Long, 122° 20.146'W)(Fig. 1; Rowe et al., 2006, 2009). Field relations of the scoria cone and lava flow indicate the Quartzville volcanism is much younger than the surrounding Western Cascades (~40-10 Ma), with the cinder cone preserved on a peak and lava filling the incised valley below (Fig. 1). Field observations are consistent with a young Ar-Ar age of 42 ka (Supplemental Table S1). The flow and cone represent a relatively small volume and isolated eruptive event. The flow thickness averages ~10m, thinning to 2m near the southern tip, with a total estimated eruptive volume of ~$4.5*10^{-3}$ km^3. Bulk samples were collected both from the lava flow interior (exposed at an old quarry site) and from the scoria cone. Whole rock characterization results in classification of the Quartzville basalt as an absarokite (Supplemental Table S2; Conrey et al., 1997) with high K_2O (3.11 wt. %) and Na_2O (2.88 wt. %) (Rowe et al., 2006; 2009). Although recent convention is to generalize the classification of these alkali rich mafic magmas as shoshonites, here we maintain the more formal definition based on whole rock geochemistry and mineralogy. Despite differences in major element composition between the scoria glass and lava whole rock, identical trace element signatures indicate the two share a common petrogenesis (Rowe et al., 2006). Whole rock Sr, Nd, Pb, Re, and Os isotopes are reported by Schmidt et al. (2008, 2013). Of particular note, Re concentrations from the Quartzville absarokite are relatively low compared to

111 other Cascade arc basalts with a concentration of 0.007 ppb (Schmidt et al., 2013) and a $^{87}Sr/^{86}Sr$
112 of 0.70382 that is more radiogenic than other Cascade basalts and basaltic andesites (Schmidt et
113 al., 2008).
114
115 **Analytical Methods**
116 **Mineral analyses.** Mineral major and minor element compositions were determined by
117 electron microprobe analysis (EMPA) on a Cameca SX 100 at Oregon State University, using a
118 15 KV, 30 nA electron beam focused to a 1 μm spot. Transects were carried out from core to rim
119 on 6 olivine grains from the lava flow and an additional 4 grains from the scoria. Olivine core-
120 rim analyses compliment olivine spot analyses taken adjacent to melt inclusions from the lava
121 (Rowe et al., 2006) and scoria (Rowe et al., 2009). Multiple analyses of San Carlos olivine (Fo_{90})
122 analyzed as a secondary standard indicate Ni and Mn analyses have a precision of 10 % while Ca
123 analyses have a precision of 14 %. Olivine X-ray maps were produced on a JEOL 8500F
124 Hyperprobe at Washington State University and on the Oregon State University CAMECA SX-
125 100. Clinopyroxene transects were made on several grains using the same beam conditions
126 utilized for olivine analyses.
127 **Oxygen isotopes.** Olivine oxygen isotope ($\delta^{18}O$) compositions were determined for a
128 suite of primitive Cascade arc, forearc, and backarc basalts, including the forearc Quartzville
129 basalt. Whole rock compositions corresponding to sample names/numbers are reported by Rowe
130 et al. (2009). Following picking, olivine grains for oxygen isotope analysis were rinsed in a sonic
131 bath of ethanol. Olivine grains selected for analysis were free from alteration as well as obvious
132 melt inclusions and/or abundant spinel (oxide) inclusions. Oxygen isotopes of olivine grains
133 were measured by CO_2 laser fluorination at California Institute of Technology on four

consecutive days following the method described by Eiler et al. (2000). San Carlos olivine grains were analyzed repeatedly over the four analytical sessions with a reproducibility of ±0.11‰ (1σ). Oxygen isotope measurements were corrected based on daily analysis of GMG-2 garnet standard (5.8‰ accepted lab value), analyzed 3-4 times a day (Supplemental Table S3). Unknown samples were analyzed 2-3 times, with sample weights from 1.8-3 mg. Several samples have isotopic ranges greater than that predicted by reproducibility of the olivine standards with up to 0.45‰ variation.

RESULTS

Petrography

Within the lava, olivine is the major phenocryst phase with microphenocrysts of clinopyroxene (grading into groundmass). Olivine are predominantly euhedral to subhedral, however many of the largest grains (up to ~500 μm) are also broken, with only a portion of the grain preserved in the thin section (Fig. 2). Jagged and embayed edges, and crystallized melt inclusions are also associated with euhedral grains. X-ray mapping indicates an increase in Mg toward the rim of olivine grains, consistent with mineral transects (Fig. 3). Abundant oxide mineral inclusions (Cr-spinel and magnetite) occur in olivine-hosted melt inclusions and within olivine grains (Cr-spinel). The abundance of magnetite and spinel inclusions in olivine is highly variable, although olivine crystals absent of inclusions are rare. Oxide inclusions are often concentrated within particular zones in olivine crystals (Fig. 2). In addition, a small proportion of olivine have an unusual symplectic texture, with magnetite apparently exsolving out of the olivine, roughly perpendicular to crystal margins. This texture becomes increasingly developed towards the interior of the olivine and is absent at grain boundaries (Fig. 2).

Clinopyroxene microphenocrysts have a maximum grain size of ~400 um, however,

crystals are predominantly smaller than 200 μm. Clinopyroxene are euhedral with distinctive zoning evident petrographically and in back-scatter imaging (Fig. 4).

The lava groundmass is composed predominantly of plagioclase and clinopyroxene with lesser magnetite and apatite. Groundmass X-ray mapping indicates abundant sulfur-bearing apatite with decreasing sulfur towards the rims.

Olivine is the only phenocryst phase observed in the Quartzville scoria with grain sizes comparable to those observed in the lava. Scoria groundmass phases proportionally are dominated by olivine > clinopyroxene > micro-apatite (Fig. 5). Notable differences of the scoria petrography to the petrography of the lava are the absence of magnetite inclusions in the olivine, and the absence of magnetite and plagioclase as groundmass phases. Petrographic characteristics of the lava and scoria are summarized in Table 1 along with the characteristic mineral geochemical variations.

Mineral chemistry

Olivine. Olivine from within the lava, ranging from $Fo_{93.8\text{-}88.6}$ (average $Fo_{90.7}$), have significantly more variability than olivine observed within the scoria which have relatively restricted compositions ($Fo_{90.6\text{-}88.2}$; average $Fo_{89.4}$) (Fig. 4; Table 1, 2). Groundmass olivine in the scoria sample has an average composition of Fo_{89}. Table 2 reports average and representative olivine analyses while the complete dataset is available as Supplemental Table S4.

Nickel concentrations in olivine phenocrysts are exceptionally high, varying from 6400-800 ppm Ni in the lava to 5500-1100 ppm Ni in the scoria (Fig. 6). Nickel concentrations do not vary linearly with olivine major element composition. Instead, the maximum Ni concentration coincides with a ~Fo_{91} olivine (Fig. 6). Nickel concentrations decrease significantly from Fo_{91} to $Fo_{88.4}$. However, while more variable, above Fo_{91} olivine Ni concentrations also decrease with

increasing forsterite content up to $Fo_{93.8}$.

Below Fo_{91}, olivine Ca concentrations are inversely correlated to Ni in olivine, with a minimum concentration of ~860 ppm Ca at Fo_{91}, increasing to 1785 ppm toward both lower and high Fo content (Fig. 6, 7). However, although correlated the relationship is non-linear. As Ni decreases from a maximum of 6380 to ~4500 ppm Ni, Ca contents in olivine have no consistent co-variation and remain relatively constant at 930 +/- 110 ppm Ca (Fig. 7). Below ~4500 ppm Ni, Ca concentrations linearly increase. Manganese concentrations decrease from 2320 to 680 ppm Mn as olivine Fo content decreases from $Fo_{93.8}$ to Fo_{91}. Below Fo_{91}, Mn is significantly more variable but generally increases toward 1500 ppm as Fo content decreases. Olivine Mn and Ca contents are broadly correlated, and Mn shares the same relationship as Ca with decreasing Ni contents.

Although groundmass olivine are less common, analysis of a groundmass/microphenocryst olivine from the scoria sample indicates the olivine is more evolved with an average composition of Fo_{89} (Fig. 5). The groundmass olivine core to rim has decreasing Ni, from 1860 to 1310 ppm, and increasing Ca, from 1605 to 1940 ppm, respectively, similar to olivine phenocryst rim compositions from both the lava and the scoria.

Olivine transects. Olivine from the lava have both normal and reverse grading toward grain rims (Table 1). Reverse Fe-Mg grading is generally only observed in the outermost 50 μm of the olivine, with Fo content increasing to ~Fo_{94}. Prior to the increase in Fo content at the rim, there is a decrease to ~$Fo_{89.5}$. Normally zoned olivine have rim compositions that match the minimum ($Fo_{89.5}$) observed in reversely zoned crystals (Fig. 8). Transects of olivine from the scoria sample are all normally zoned and show no evidence for the increase in Fo content in the grain boundaries with a rim composition varying from $Fo_{88.7}$ to $Fo_{89.4}$ (Fig. 8). Regardless of

olivine rim composition (Fo content), Ni concentrations systematically and significantly decrease over the outer 100-200 μm of the grains, from ~6000-5000 ppm Ni in the core to 2000-1000 ppm Ni in the rims (Fig. 8). The same pattern is observed in olivine from the scoria although maximum Ni concentrations in the grain cores are substantially lower, generally < 4000 ppm Ni (Fig. 8). Ca concentrations in olivine are again independent of olivine rim variation (Fo content) and vary from 800-1000 ppm Ca throughout most of the olivine but increase to as high as 1750 ppm Ca at the grain margin, the mirror image of Ni variation in olivine in the outer 100-200 μm of the olivine. Manganese variations in olivine transects are less discernable (Fig. 3).

Clinopyroxene. Clinopyroxene phenocryst transects all have irregular Fe-Mg oscillatory zoning. The same Fe-Mg zoning is evident both in larger microphenocrysts and in groundmass clinopyroxene, with high-Fe rims indicated from X-ray mapping. The full chemical analysis of clinopyroxene is available in Supplemental Table S5. The Mg# of clinopyroxene phenocrysts ranges from 82 to 89. Groundmass clinopyroxene have an average core Mg# of 86.2 ± 1.5, compositionally similar to larger phenocrysts. Despite the elevated Ni concentrations in olivine, Ni in clinopyroxene is below detection limit (~450 ppm). Fe_2O_3 in clinopyroxene is calculated stoichiometrically. Although clinopyroxene compositions are variable, nearly all transects indicate an increase in Fe_2O_3/FeO at the grain rims (Fig. 4).

Olivine oxygen isotopes. Duplicate analyses of oxygen isotopes from olivine crystals recovered from the Quartzville lava flow give identical $\delta^{18}O$ values of 5.64‰. Other basalt types identified by Rowe et al. (2009), including calc-alkaline, low-K tholeiite, and enriched-intraplate basalts (or OIB-like), have $\delta^{18}O$ ranging from 5.5 to 5.2‰ in Central Oregon with an average of 5.34‰, significantly lower than the Quartzville basalt (Fig. 9). The variability observed within the other Central Oregon basalts is dominantly within the range for upper mantle olivine (5.2 ±

226 0.2; Mattey et al., 1994; Eiler et al., 2000), and does not correlate to basalt major element
227 composition (Fig. 9). Oxygen isotope analyses of Central Oregon Cascade forearc, arc, and
228 backarc basalts are available in Supplemental Table S3.

229 **Melt compositions.** Supplemental Table S2 summarizes the whole rock/melt
230 compositions from melt inclusions, scoria glass, and lava samples including new analyses of
231 scoria glass and compositions reported by Rowe et al. (2006, 2009). Scoria glass is
232 compositionally variable, with MgO and CaO decreasing with increasing SiO_2, as a result of
233 varying amounts of fractional crystallization of clinopyroxene ± olivine during eruption. Scoria
234 glass MgO wt. % ranges from 4.3 to 4.8 wt. % compared to 6.7 wt. % in olivine-hosted
235 inclusions calculated to be in equilibrium with their host olivine (Rowe et al., 2009) and 9.86 wt.
236 % MgO in the whole rock lava (Rowe et al., 2006). Olivine compositions adjacent to melt
237 inclusions in olivine from the lava range from $Fo_{89.4\text{-}92.2}$ and from $Fo_{86.1\text{-}90.2}$ from the scoria
238 (Rowe et al., 2006). No groundmass glass was evident in the lava sample. High MgO in the
239 whole rock has previously been ascribed to olivine accumulation (Rowe et al., 2006). FeO* (total
240 Fe) from the lava whole rock and scoria glass is uniformly low, with a limited range in
241 concentrations from 6.3 to 6.5 wt. % FeO* and olivine-hosted melt inclusions from the scoria
242 with 6.7 wt. % FeO*. Importantly, all four materials (lava, scoria, and olivine-hosted melt
243 inclusions in the lava and scoria), have the same relative trace element variability (Fig. 10). All
244 samples are extremely enriched in large ion lithophile elements (LILE's) and light rare earth
245 elements (LREE's) and comparably depleted in high field strength elements (HFSE; especially
246 Nb and Ta) and heavy rare earth elements (HREE's). The whole rock Ni concentration is 256
247 ppm compared to 13.9 ppm in the scoria glass. Trace element characteristics of the lava are
248 adakite-like (Defant and Drummond, 1990), with normalized Dy/Yb and La/Yb of 3 and 53.5,

249 respectively, and a Sr/Nd of 31.2 with a Sr/Y of 151.

250

251 **DISCUSSION**

252 **Mantle Xenocrystic Olivine?**

253 The anomalous olivine compositions in the Quartzville basalt and scoria have the
254 potential to provide important constraints on the origin and petrogenesis of the magma. First,
255 however, non-magmatic origins (i.e. mantle xenocrysts) for the olivine must be ruled out.
256 Although most of the olivine grains have euhedral textures (Fig. 2), this does not
257 necessitate a magmatic origin, as euhedral rims can mantle xenocrystic olivine (e.g. Kamenetsky
258 et al., 2008; Arndt et al., 2010; Pilbeam et al., 2013). The unique magnetite exsolution texture
259 identified in a small proportion of grains may suggest a xenocrystic origin for this population of
260 grains- note that the grain margin is free from magnetite exsolution and may reflect olivine rim
261 crystallization (Fig. 2). However, the mineral composition is identical between these particular
262 grains with exsolution textures and cores of other olivine grains, which lack this texture, and
263 would suggest a common origin for the cores of most of the olivine grains despite the presence
264 or absence of this texture. The observed exsolution texture could result from a change to more
265 oxidizing magmatic conditions, resulting in a reduction of the olivine stability field (Muan and
266 Osborn, 1956), and a subsolidus exsolution of magnetite. This interpretation is consistent with
267 the high oxidation state (> FMQ + 1.5) of the erupted magma (Rowe et al., 2009). In contrast, the
268 presence of melt embayments and silicate melt inclusions supports a magmatic origin for these
269 olivine. Olivine-hosted melt inclusion trace element compositions from both the lava and scoria
270 match that of their respective host rocks that not only suggests a magmatic origin but that the
271 melts are related (Rowe et al., 2006; 2009). As stated above, melt inclusions are found in up to

272 Fo_{92} olivine from the lava, implying a magmatic origin for most olivine grains.

273 Although mantle xenoliths are rare in the Cascades, Ni contents from harzburgite and
274 websterite xenoliths from Simcoe Volcano, in the Washington Cascades, range from ~1885 –
275 3380 ppm Ni (Brandon & Draper, 1996). Olivine Ni contents from Quartzville are significantly
276 greater than observed in peridotitic olivine, with cores typically ranging from 4500 – 6380 ppm
277 Ni. These concentrations are well above typical mantle-derived olivine (generally below 3800
278 ppm Ni), also strongly favoring a magmatic origin for these olivine (Fig. 7; e.g. Kamenetsky et
279 al., 2006; Elburg et al., 2006; Sobolev et al., 2007; Straub et al., 2008).

280 Early studies of low-Ca olivine suggested that many of these olivine were derived from
281 mantle peridotites (e.g., Simkin and Smith, 1970). However, more recent examination into low-
282 Ca olivine has identified numerous occurrences of magmatic low-Ca olivine (e.g., Kamenetsky
283 et al., 2006). When compared to mantle peridotite olivine, where Ca contents are generally below
284 700 ppm, Ca concentrations in Quartzville olivine are enriched (Fig. 7). In these examples of
285 magmatic occurrences, low-Ca (< 1070 ppm Ca) olivine are often associated with high-Ni (up to
286 3930 ppm Ni) contents in high-Fo olivine.

287 Consistent with an inferred magmatic origin of olivine from textural and trace element
288 data, $\delta^{18}O$ of the high-Ni olivine (5.64 ± 0.1‰) are greater than the values attributed to mantle
289 peridotite which range from 4.8 – 5.5‰ (average of 5.18 ± 0.28‰; Mattey et al., 1994). It could
290 be argued that if the olivine cores are of mantle origin (xenocrystic), with magmatic rims, bulk
291 olivine isotopic analysis would reflect a mixture of the two components. Oxygen isotopic
292 analysis of other primitive basalts in the Oregon Cascades, however, are all within error of
293 “mantle olivine” (Mattey et al., 1994). If rim olivine growth was altering the isotopic
294 composition of the Quartzville olivine, we would predict that the measured $\delta^{18}O$ would be a

minimum value and thus the original olivine core isotopic value would be even further removed from the previously defined mantle olivine compositional range.

Overall, multiple lines of evidence, textural and compositional, support the conclusion that high-Fo, high-Ni, low-Ca olivine are not simply transported mantle xenocrysts. Therefore, understanding the origin of these anomalous olivine will provide constraints on the magma petrogenesis for this unusual forearc magmatism.

Olivine-melt equilibrium and partitioning

Fe-Mg olivine-melt equilibrium. Major element compositions of re-homogenized olivine-hosted melt inclusions for the Quartzville lava were previously deemed to be unreliable (Rowe et al., 2006). However, from melt inclusion trace elements (Rowe et al., 2006; Rowe et al., 2009) and field relations, we can conclude that scoria and lava samples are genetically related. From this relationship, we can reassess the olivine-melt Fe-Mg equilibrium. A ferrous-ferric ratio ($Fe^{3+}/\Sigma Fe$ of ~0.32) is calculated using the algorithm of Sack et al. (1980) from the calculated fO_2 (fO_2 of ~ ΔFMQ +1.5-1.9; Rowe et al., 2009; Jugo et al., 2010), the scoria glass composition, and an assumed temperature of 1115°C (Rowe et al., 2006). With an olivine-melt $Kd^{Fe\text{-}Mg}$ of 0.30 ± 0.03 after Roedder and Emslie (1970) and the same $Fe^{3+}/\Sigma Fe$ between the scoria and lava, we can make the assumption that the average melt inclusion composition from the scoria, trapped in olivine with an average $Fo_{89.4}$ olivine composition, is equivalent to the melt composition that is in equilibrium with $Fo_{89.4}$ olivine from the lava. This olivine composition matches the minimum Fo content in the olivine profiles prior to the spike in Fo content to $Fo_{93.8}$ at the olivine rims (Fig. 8).

This new assessment of Fe-Mg equilibrium suggests that the high MgO wt. % of the lava (9.8 wt. % MgO) is the result of approximately ~7.8 wt. % olivine accumulation, consistent with

prior estimates of olivine accumulation (Rowe et al., 2006). Two important conclusions come from these observations. First, if the olivine core to near-rim variation in olivine forsterite content is the result of fractional crystallization, this would imply a minimal amount of fractionation to get from ~Fo_{91} to ~Fo_{89}. Second, the presence of accumulated olivine must be taken into account for any petrogenetic model. The question must then become what is the origin for the accumulated olivine. This question, and the high Fo content olivine rims (> Fo_{91}) are discussed further below.

Ni and Ca olivine-melt partitioning. Nickel and Ca partitioning in olivine provides an opportunity to assess the evolution of olivine crystals in the melt on the basis of a fractional crystallization model. Assuming a final melt composition similar to that of the scoria olivine-hosted melt inclusions with equilibrium $Fo_{89.4}$ olivine and an Fe^{3+}/Fe_{Total} of 0.32, only 3 wt. % of equilibrium olivine needs to be added back to the melt for an Fo_{91} olivine to be the equilibrium olivine composition. Note we do not use the scoria glass composition here because of the slight disequilibria between scoria glass and rim olivine discussed above. Overall, this model suggests a minimal amount of olivine fractionation is recorded in the Fe-Mg variation of the crystals and forms the basis for the following discussion.

Prior studies have documented that the abundance of Ca in olivine is a function of olivine Fo content, pressure, and melt composition (e.g., Stormer, 1973; Libourel, 1999; Jurewicz and Watson, 1988). Experimental absarokitic run products suggest a slight decrease in Ca in olivine partitioning with increasing magmatic water content, from ~0.029 to 0.024 (Hesse and Grove, 2003). However, partition coefficients calculated from experimental run products are higher than used in our modeling. Calculated olivine trace element compositions using these partition coefficients would be even further removed from observed low-Ca variations. Using average

inclusion and olivine compositions for the scoria we can define a partition coefficient $D_{Ca}^{ol\text{-}melt}$ of 0.017. Given the minimal olivine fractionation and thus little change to a theoretical melt composition, we can assume a nearly constant partition coefficient for Ca in olivine. This calculated value is similar to that predicted by Jurewicz and Watson (1988) for high-Fo basalts (e.g., 0.016). In an olivine-dominated crystallizing assemblage, CaO in the melt will remain nearly unchanged (< 0.5 wt. % CaO increase) for the small amount of olivine crystallization we predict. The effect is even more pronounced with the addition of clinopyroxene fractionation which will reduce the abundance of CaO available in the melt with continued crystallization. Given the incompatible behavior of Ca in olivine and its dependence on CaO in the melt (e.g. Jurewicz and Watson, 1988), we cannot explain the ~ 1000 ppm increase in Ca in olivine from core to rim with a simple fractionation model (Fig. 7a).

Experimental studies have long identified that Ni olivine-melt partition coefficients are strongly dependent on melt composition (both as a function of MgO content and melt polymerization) and temperature (e.g., Hart and Davis, 1978; Leeman and Lindstrom; 1978; Kinzler et al., 1990; Beattie et al., 1991; Wang and Gaetani, 2008; Li and Ripley, 2010). However, these two parameters have proven difficult to deconvolve, given the interdependence of temperature and melt composition (Hart and Davis, 1978; Li and Ripley, 2010). For the scoria melt, with a Ni melt concentration of ~14 ppm, and olivine rim compositions we obtain reasonably good agreement between MgO-dependent algorithms ($D_{Ni}^{ol\text{-}melt}$ of 25.6-30.6; Hart and Davis, 1978; Kinzler et al., 1990) and more compositional and temperature dependent algorithms ($D_{Ni}^{ol\text{-}melt}$ of 26.3; Li and Ripley, 2010) for Ni in olivine partitioning. Since this represents the most evolved melt composition, following the MgO-dependent partitioning behavior, these calculated D's are maximum values. Unlike Ca, the highly compatible nature of Ni in olivine

means that fractionation of olivine will have a significant effect on Ni melt contents and subsequent olivine crystallization.

Using the same methodology described for Ca above, Ni contents in olivine can drop by ~2500 ppm, even with the minimal anticipated olivine fractionation. As stated, this would represent a maximum change in Ni since the more primitive (by ~1 wt. % MgO) theoretical starting melt composition would result in a lower Ni in olivine partition coefficient (e.g. Hart and Davis, 1978; Leeman and Lindstrom 1978). However, while this model can explain much of the variation in Ni in olivine, it does not account for Ni concentrations as low as 1000 ppm observed near grain boundaries (Fig. 6, 7). From this modeling, it is apparent that the co-variation in olivine Ni and Ca concentrations cannot be reasonably explained using a fractional crystallization model with olivine evolving from ~Fo_{91} to ~Fo_{89} compositions (Fig. 7).

Paradoxical compositions

Modeling of olivine compositions, particularly for Ni and Ca in olivine, indicates olivine core compositions cannot be generated from the melt in which they are transported by simple fractional crystallization. The variations we observe in olivine profiles are instead more consistent with diffusive re-equilibration following incorporation of olivine grains into a more Ca-rich, Ni-poor melt, as similarly observed by Kamenetsky et al. (2006). The presence of low-Ca magmatic olivine are typically attributed to crystallization from a low-Ca melt (e.g., Kamenetsky et al., 2006; Elburg et al., 2006). Although the re-homogenized major element compositions of olivine-hosted melt inclusions from the lava are compromised due to Fe-dilution, elements not strongly controlled by olivine crystallization/dissolution have far greater variability than predicted from heating experiments (Rowe et al., 2006). This is especially true of CaO, with 5 wt. % variation (from ~ 8 – 13 wt. % CaO) reported in inclusions minimally

effected by Fe-dilution (rehomogenized between 1125-1150°C; Rowe et al., 2006). Taken qualitatively, re-homogenized olivine-hosted melt inclusion compositions from the lava may, in fact, provide evidence of a low-CaO, high-SiO_2 (up to 54 wt. % SiO_2) melt component not observed in either scoria glass or olivine-hosted inclusions from the scoria.

Melt inclusion, groundmass scoria glass, and lava whole rock trace elements all have the same overall distribution patterns (Rowe et al, 2006; 2009), and indicate a related petrogenesis. This is inconsistent with the inferred disequilibrium and melt heterogeneity indicated by mineral chemistry and re-homogenized melt inclusion major element compositions. Hesse and Grove (2003), propose that for Mexican volcanic belt absarokites, trace elements record a deeper, "original" source, while major elements instead record later re-equilibration between the original melt and shallower hot mantle. In order to explain two melts with different major element characteristics but similar trace element signatures, we propose a similar model whereby incompatible trace elements record the original slab-derived fluid-rich melt but subsequent metasomatism and re-equilibration impart this trace element signature on a mineralogically variable (veined?) subarc mantle.

Nature of sources

The origin or cause of enriched Ni concentrations in olivine is variably ascribed to different mantle sources (including eclogitic and pyroxenitic domains) and/or magmatic compositions and oxidation states and therefore is of great interest as a potential constraint on intrinsic magma properties and/or mantle source domains (e.g., Davis and Smith, 1993; Sobolev et al., 2007; Straub et al., 2008; Wang and Gaetani, 2008). High-Ni olivine have been identified in several volcanic arcs in addition to the Cascades, including Japan, Kamchatka, and the Mexican volcanic belt (Straub et al., 2008; Tatsumi et al., 2006; Ishimaru and Arai, 2008).

410 However, to date no single model readily explains all of the observed occurrences of high-Ni
411 magmatic olivine. Given the compositional variability of the host lavas and the widespread and
412 diverse localities at which anomalous olivine are observed it is perhaps not surprising that the
413 origins of these olivine are debated.

414 Prior efforts at understanding the genesis of high-Ni magmatic olivine have focused on two
415 main processes altering Ni partitioning behavior. All models require modification of the mantle
416 peridotite source or primitive basalts through addition of a silicic component (e.g. an eclogitic
417 melt or siliceous subduction component). It is proposed that addition of a siliceous component to
418 the mantle source results in the conversion of olivine to pyroxene (e.g., $SiO_2 + Mg_2SiO_4 =$
419 $Mg_2Si_2O_6$; Sobolev et al., 2005, 2007; Straub et al., 2008). Sobolev et al. (2005, 2007) argue that
420 conversion to a pyroxene-dominant source lithology changes the buffering of trace elements (e.g.
421 the bulk partition coefficient for Ni in pyroxene is lower than for Ni in olivine), allowing primary
422 basaltic melts to have higher Ni contents, reflected then in subsequent olivine crystallization.
423 However, the partition coefficient of Ni in olivine has been demonstrated to strongly increase
424 with melt polymerization and decreasing MgO content (Leeman and Scheidegger, 1977; Hart
425 and Davis, 1978; Leeman and Lindstrom, 1978; Kinzler et al., 1990; Li and Ripley, 2010).
426 Although starting from a similar reacted mantle source, Straub et al. (2008) argues that a melt
427 generated from a pyroxenite source, with higher SiO_2 and lower MgO, will therefore result in
428 higher Ni in the crystallizing olivine because of the increase in Ni in olivine partitioning (i.e.
429 without a significant change to the primary melt Ni content). Alternatively, Wang and Gaetani
430 (2008) suggest that because of the effect of melt polymerization on Ni in olivine partitioning,
431 you do not need a reaction-pyroxene dominant lithology and that simply adding eclogitic partial
432 melts to tholeiitic basalts promotes crystallization of relatively high-Ni olivine. Despite

433 variations, all models require fundamental changes to either primitive basalt compositions or
434 mantle source lithologies and thus the origin of these chemically anomalous high-Ni olivine can
435 provide significant constraints on magma petrogenesis and evolution.

436 A mineralogically distinctive source (i.e. non-peridotitic) is consistent with olivine $\delta^{18}O$
437 (5.64 ± 0.1 ‰), greater than that typically observed in mantle peridotite olivine or peridotite-
438 derived magmatic olivine. Given the primitive nature of the olivine phenocrysts, it is unlikely
439 that these isotopically heavy $\delta^{18}O$ values are the result of crystallization or crustal contamination,
440 both of which may slightly increase $\delta^{18}O$ in basalts (Bindeman et al., 2004; Harmon and Hoefs,
441 1995). In the following discussion we propose two possible sources of pyroxene-dominated
442 lithologies.

443 Glass trace element signatures with very low Yb (1.2 ppm) and Y (20 ppm), and high
444 $[Dy/Yb]_N$ (3), are consistent with a residual garnet phase in the source region (Fig. 10). One
445 obvious potential source for garnet is in ecologitized subducted oceanic crust at depths greater
446 than 45 km in the down-going Juan de Fuca Plate (Bostock et al., 2002). Given the young (~8
447 Ma) and hot nature of the subducting plate (Stein and Stein, 1996; Syracuse et al., 2010), a low
448 degree partial melt of ecologitic crust is not unreasonable. Heavy $\delta^{18}O$ isotopic signatures in
449 olivine, similar to the Quartzville olivine, are found in many arc settings worldwide, and are
450 often attributed to a number of different processes including melting of de-serpentinized mantle
451 and slab melting (e.g., Bindeman et al., 2005; Eiler et al., 2005; Johnson et al., 2009; Auer et al.,
452 2009). Quartzville olivine oxygen isotopic signatures are also similar to high-Mg andesites from
453 the Cascades ($\delta^{18}O$ 5.49 – 5.78‰), suspected of containing a slab melt component (Bindeman et
454 al. 2005). If the high $\delta^{18}O$ isotopic signature of the olivine were inherited from the subducting
455 plate, this may indicate that the fluid came from the upper part of the oceanic crust, altered by

456 seawater at low temperature (Muehlenbachs, 1986; Auer et al., 2009). However, Bindeman et al.
457 (2005) compiled oxygen isotopic analyses from world-wide adakites thought to be related to slab
458 melting, and this study suggests that isotopic exchange between slab melts and the mantle wedge
459 may buffer the variability observed in olivine such that the location within the subducting plate
460 where melting is taking place is more difficult to reconcile.

461 High-Mg dacitic magmas, thought to be derived from partial melting of the subducting
462 plate (adakites), have characteristic trace element signatures with high Sr concentrations and
463 La/Yb ratios (e.g., Kay, 1978). Despite melt trace element similarities, the major element
464 composition of the lava, glasses and melt inclusions, including the qualitative higher SiO_2, lower
465 CaO re-homogenized inclusions, are not evolved enough to resemble a typical adakitic slab melt.
466 However, similar to the two-stage model of Hesse and Grove (2003), the subducting plate could
467 represent the original source of the trace element signature.

468 Following the generation of a siliceous subduction component, ascent and metasomatism
469 of the overlying peridotitic mantle could result in a pyroxene-dominated lithology as olivine is
470 converted to orthopyroxene (e.g., Straub et al., 2008). As previously introduced, from various
471 models it has been proposed that melts generated from this reaction-pyroxene dominant source
472 lithology could produce melts with fundamentally higher Ni contents (Sobolev et al., 2005,
473 2007) or have higher SiO_2 and lower MgO (Straub et al., 2008). The resultant olivine
474 crystallization from reaction-pyroxene dominant source lithologies in either case would be
475 relatively high in Ni compared to those crystallizing from peridotite-derived magmas. This
476 change in Ni behavior could occur because of both lower Ni partition coefficients in pyroxene
477 compared to olivine (Sobolev et al., 2005, 2007) and increasing Ni in olivine partitioning with
478 melt polymerization and decreasing MgO (Straub et al., 2008). While our results cannot

479 necessarily distinguish between these two mechanisms of Ni enrichment, both may be impacting
480 observed olivine compositions. The correlation between high-Ni and low-Ca in olivine is
481 consistent with a change in source mineral buffering, while the qualitatively higher melt SiO_2 at
482 low MgO contents in rehomogenized inclusions favors a melt polymerization control on Ni
483 partitioning.

484 Sobolev et al. (2007) further investigated the mineralogical response to pyroxenite versus
485 peridotite melting, indicating that pyroxenite melts characteristically have high Ni/Mg
486 (100*Ni/Mg of ~1.5-2.5) and low Ca/Fe (100*Ca/Fe of ~2-2.5) at low Mn/Fe (100*Mn/Fe of
487 ~1.1-1.3). While Mn/Fe ratios are not as well constrained in the present study, for the range of
488 $Fo_{91\text{-}89.5}$ (excluding high-Fo and low-Fo rim growth), we observe olivine compositions near the
489 pyroxenite-melt field with average 100*Ni/Mg, 100*Ca/Fe, and 100*Mn/Fe of 1.39, 1.39 and
490 1.34, respectively (Fig. 7b).

491 Although olivine cores are thought to record crystallization from a melt of a pyroxenite-
492 dominated source lithology, diffusive re-equilibration on the olivine rims (higher Ca and lower
493 Ni), coupled with a change in major element melt composition recorded by the host lava and
494 glasses, suggests olivine grains record a mixing event. Prior trace element modeling has
495 suggested the Quartzville basalt could be generated by high significant fluid fluxing (up to 6 wt.
496 % of a hydrous subduction component) of a highly depleted mantle peridotite which had
497 previously undergone ~25 % melting (Rowe et al., 2009). A mixing based model to explain the
498 core-rim variation in olivine is also consistent with observations of magma production from the
499 Mexican Volcanic Belt (Straub et al., 2008, 2011).

500 The change in source mineralogy, from a pyroxenite-dominated to a depleted harzburgitic
501 peridotite, can be produced following the model of Straub et al. (2008) whereby the addition of a

502 SiO_2-rich subduction component to the mantle wedge will result in vertical zones of pyroxenite,
503 surrounded by depleted mantle. However, as discussed above, trace elements derived from the
504 subducted plate would reflect the original garnet-bearing source and may rapidly re-equilibrate
505 as a result of their high abundances relative to the surrounding mantle (Hesse and Grove, 2003;
506 Straub et al., 2008; Straub et al., 2014). The result would be a mantle source containing both
507 reaction-pyroxenite and highly fluid-fluxed, depleted peridotitic mantle (Fig. 11). Initial melt
508 production in the pyroxenite zone, and subsequent olivine crystallization, would result in olivine
509 with high Ni and low Ca. Later melts of the fluid-fluxed, depleted mantle incorporating early
510 pyroxenite-derived olivine would explain the similarity in incompatible trace element
511 abundances in the melt inclusions as well as host lava and scoria, despite the disequilibrium in
512 olivine composition resulting from olivine overgrowth and diffusive re-equilibration with the
513 peridotite-derived melt.

514 The magma mixing scenario of Wang and Gaetani (2008) could be proposed as an
515 alternative model to that proposed above. However, a magma mixing model with no fundamental
516 change to the source lithology could explain the olivine compositional variations, but not the
517 nearly identical melt trace element compositions between melt inclusions, lava, and scoria. For
518 all of our observations to be true, we need to have a mineralogically variable source that has been
519 overprinted with the same incompatible trace element signature. Importantly, this implies that
520 the source of the unique olivine chemistry is in the subarc mantle wedge, while the origin of the
521 enriched trace element signature is the subducting plate.

522 **Olivine rim growth**

523 The last aspect of the anomalous olivine compositions to be explained are the very high
524 forsterite rim compositions (Fo_{91-94}). Two main mechanisms may provide an explanation for the

very high forsterite (>Fo_{91}) olivine near the rims of the olivine grains in the lava. First, the mixing event discussed above may result in equilibrium crystallization of the very high Fo olivine rims. However, Fe-Mg equilibrium calculations suggest Fo_{86} olivine should be in equilibrium with the host melt (consistent with the lowest recorded Fo content prior to the high Fo olivine rim). In addition, despite the similar glass/whole rock trace element signatures and identical Ni-Ca in olivine rim co-variation, high Fo rims are not observed on olivine from the scoria. The highest Ni concentrations are not observed in the high-Fo olivine, and Ni concentrations systematically, and nearly linearly, decrease toward the olivine rim regardless of the switch from normal to reverse Fe-Mg zoning in olivine from the lava. Olivine grains from the scoria, where no reverse zoning is observed, display the same trend in Ni decreasing steadily toward the rim (Fig. 3). Similarly, Ca concentrations increase towards the rim in olivine crystals of both the lava and scoria, irrespective of the normal or reverse Fe-Mg zoning. The high olivine Fo contents (> Fo_{91}), therefore, are unique to the lava flow, despite a similar petrogenic history between the lava and scoria. This suggests the high-Fo rims may be related to eruptive processes.

A second potential mechanism for causing the high Fo contents and reversed Fe-Mg zoning in the outer 25-50 μm is an increase in the oxidation state during slow cooling of the lava. Assuming melt composition remains unchanged, in order to crystallize an $Fo_{93.8}$ olivine from the average scoria MI composition (Supplemental Table S2), Fe^{3+}/Fe_{Total} would need to increase to 0.62, corresponding to an oxidation state of approximately +4.6 log fO_2 (ΔFMQ). While this oxidation state is high relative to other basalts in the Cascades which are generally at or below FMQ (Rowe et al., 2009), it corresponds well with estimated oxidation states for minettes from the western Mexico Volcanic Belt which vary from +3.4 to +7 log fO_2 (ΔFMQ; Wallace and Carmichael, 1989).

548 As previously mentioned, spinel composition in the lava ranges from a high-Cr to high-
549 Fe end member (compositional data presented by Rowe et al. (2006) are provided in
550 Supplemental Table S6). As calculated temperature and Mg# decreases, the Fe component, and
551 calculated oxidation state also increase (Ballhaus et al., 1991). Calculated oxidation states in the
552 lowest temperature spinels are up to +4.1 log fO_2 (ΔFMQ), similar to the predicted +4.6 log fO_2
553 (ΔFMQ) from olivine compositions required to produce the high Fo olivine rims. The low-T,
554 high-Fe spinels likely reflect low-T re-equilibration (Kamenetsky et al., 2001). However, this re-
555 equilibration may also be a function of increasing oxidation state of the lava upon cooling and
556 degassing.
557 Interestingly, Wallace and Carmichael (1989) also argue that oxidation of the western
558 Mexico Volcanic Belt minettes is a rapid, late process and that pre-eruptive fO_2 was
559 approximately +3.2-3.7 log fO_2 (ΔFMQ). A late oxidation model fits well with our mineralogical
560 observation of high Fo olivine rims only observed on olivine in the dense, more crystalline lava
561 but not on olivine from the rapidly quenched scoria. Additionally, the observed increase in
562 Fe^{3+}/Fe^{2+} calculated for clinopyroxene rims compositions from the lava is consistent with a late
563 oxidation event (Fig. 4). Wallace and Carmichael (1989) propose that oxidation is related to
564 volatile degassing, specifically the loss of H_2 derived from H_2O, based on observations and
565 similar arguments from pillow lavas where pillow interiors have a higher Fe^{3+}/Fe_{Total} versus
566 exterior glassy rinds (Christie et al., 1986). Alternatively, Metrich et al. (2009) argue that the
567 reduction of sulfur in initially oxidized systems will result in further oxidation of the melt during
568 degassing. In this case $SO_4^{2-}{}_{(melt)}$ (S^{6+}) reduces to $SO_{2\,(gas)}$ (S^{4+}) such that 1 mol of sulfate may
569 oxidize 2 mol Fe^{2+}.
570 Using the variably degassed melt inclusions from the scoria as a proxy for degassing

behavior in the lava we can evaluate the effect of degassing on the oxidation state of the magma (note that Rowe et al., 2006 report similarly high S melt contents for melt inclusions). Melt inclusions from the scoria have a maximum concentration of ~0.6 wt. % S (~87 % S^{6+}/S_{Total}) while the scoria has a minimum concentration of 0.26 wt. % S (Rowe et al., 2009). Rowe et al. (2007) demonstrated that for this scoria composition as degassing progresses (decreasing sulfur concentration) the proportion of sulfate decreases linearly and the amount of sulfur, as sulfide in the melt, stays relatively constant. This reduction of sulfate equates to a loss of 0.011 mol S^{6+} for every 100 g of magma, allowing for the oxidation of ~0.022 mol Fe^{2+} per 100 g of melt. Based on the average inclusion composition described above, for every 100 g of magma there is approximately 0.064 mol Fe^{2+} (assuming the same Fe^{3+}/Fe_{Total} of 0.32). In order to generate the highest Fo rim olivine from the same melt composition, we require Fe^{3+}/Fe_{Total} of 0.62 or the oxidation of an additional 0.028 mol Fe^{2+} per 100 g of magma. Therefore nearly all of the oxidation of the Fe needed to explain the dramatic increase in olivine rim compositions can be accommodated by reduction and degassing of oxidized sulfur (S^{6+}) and subsequent Fe oxidation ($Fe^{2+} \rightarrow Fe^{3+}$). If we assume that melt inclusions from the scoria represent an initial sulfur content for the scoria and lava melt compositions, then we can explain the lacking of high-Fo rims on olivine from the scoria simply reflecting faster cooling of the scoria upon eruption compared to the slowly cooled lava. This would imply, based on observations at Quartzville, that degassing of extremely high concentrations of oxidized sulfur must be coupled with slow cooling of the mafic magma to produce the high-Fo olivine rims.

IMPLICATIONS

Understanding the petrogenesis of the compositionally anomalous olivine from the Quartzville absarokite has significant implications for Cascade arc magma genesis, and more

broadly, subduction zone processes. Our results imply that an end-member of Cascade arc magmatism is derived from slab melting and the re-equilibration of that melt with the mantle wedge. Significant to subduction zone processes in general, our results suggest that siliceous slab melts may re-equilibrate with the sub-arc mantle, resulting in a mineralogical change while imprinting a more widespread trace element signature to the mantle wedge. Important to magma genesis, these results suggest that the mineralogical reactions (i.e. conversion of olivine to pyroxene) occurring in the mantle wedge may be decoupled from more classical trace element subduction signatures derived from the subducting plate. A similar process has been suggested in other volcanic arcs (e.g., Hesse and Grove, 2003; Straub et al., 2008; 2011; 2014) and may therefore imply a more widespread subduction zone process, often over-looked because of the relatively small volume of this magmatic composition.

ACKNOWLEDGEMENTS

We would like to thank John Eiler for assistance with gathering oxygen isotope data. Discussions with B. Leeman, M. Clynne, A. Kent, and R. Nielsen, assisted with formulating models of magma genesis at Quartzville. Reviews of an earlier manuscript by S. Straub and G. Gaetani were of great help, as were manuscript reviews by G. Zellmer and V. Kamenetsky. Partial support of funding came from NSF EAR 0440382, the Oregon State University Electron Microprobe Laboratory, and Washington State University Geoanalytical Laboratory.

REFERENCES

Arndt, N.T., Guitreau, M., Boullier, A.-M., Le Roex, A., Tommasi, A., Cordier, P., and Sobolev, A. (2010) Olivine, and the origin of kimberlite. Journal of Petrology, 51 (3), 573-602.

Auer, S., Bindeman, I., Wallace, P., Ponomareva, V., and Portnyagin, M. (2009) The origin of hydrous, high-$\delta^{18}O$ voluminous volcanism: diverse oxygen isotope values and high magmatic water contents within the volcanic record of Klyuchevskoy volcano, Kamchatka, Russia. Contributions to Mineralogy and Petrology, 157, 209-230.

Ballhaus, C., Berry, R.F., and Green, D.H. (1991) High pressure experimental calibration of the olivine-orthopyroxene-spinel oxygen geobarometer: implications for the oxidation state of the upper mantle. Contributions to Mineralogy and Petrology, 107, 27-40.

Beattie, P., Ford, C., and Russell, D. (1991) Partition coefficients for olivine-melt and orthopyroxene-melt systems. Contributions to Mineralogy and Petrology, 109, 212-224.

Bindeman, I.N., Ponomareva, V.V., Bailey, J.C., and Valley, J.W. (2004) Volcanic arc of Kamchatka: a province with high-$\delta^{18}O$ magma sources and large-scale $^{18}O/^{16}O$ depletion of the upper crust. Geochimica et Cosmochimica Acta, 68 (4), 841-865.

Bindeman, I.N., Eiler, J.M., Yogodzinski, G.M., Tatsumi, Y., Stern, C.R., Grove, T.L., Portnyagin, M., Hoernle, K., and Danyushevsky, L.V. (2005) Oxygen isotope evidence for slab melting in modern and ancient subduction zones. Earth and Planetary Science Letters, 235, 480-496.

Borg, L.E., Clynne, M.A., and Bullen, T.D. (1997) The variable role of slab-derived fluids in the generation of a suite of primitive calc-alkaline lavas from the southernmost Cascades, California.

640 The Canadian Mineralogist, 35, 425-452.
641
642 Bostock, M., Hyndman, R., Rondenay, S., and Peacock, S. (2002) An inverted continental Moho
643 and serpentinization of the forearc mantle. Nature, 417, 536-538.
644
645 Brandon, A.D., and Draper, D.S. (1996) Constraints on the origin of the oxidation state of mantle
646 overlying subduction zones: an example from Simcoe Washington, USA. Geochimica et
647 Cosmochimica Acta, 60, 1739-1749.
648
649 Christie, D.M., Carmichael I.S.E., and Langmuir, C.H. (1986) Oxidation states of mid-ocean
650 ridge basalt glasses. Earth and Planetary Science Letters, 79, 397-411.
651
652 Conrey, R., Sherrod, D., Hooper, P., and Swanson, D. (1997) Diverse primitive magmas in the
653 Cascade arc, Northern Oregon and Southern Washington. The Canadian Mineralogist, 35, 367-
654 396.
655
656 Davis, L.L., and Smith, D. (1993) Ni-rich olivine in minettes from Two Buttes, Colorado: A
657 connection between potassic melts from the mantle and low Ni partition coefficients.
658 Geochimica et Cosmochimica Acta, 57, 123-129.
659
660 Eiler, J.M., Carr, M.J., Reagan, M., and Stolper, E. (2005) Oxygen isotope constraints on the
661 sources of Central American arc lavas. Geochemistry, Geophysics, Geosystems, 6, doi:
662 10.1029/2004GC000804.

Eiler, J.M., Crawford, A., Elliott, T., Farley, K.A., Valley, J.W., and Stopler, E.M. (2000) Oxygen isotope geochemistry of oceanic-arc lavas. Journal of Petrology, 41, 229-256.

Elburg, M., Kamenetsky, V.S., Nikogosian, I., Foden, J., and Sobolev, A.V. (2006) Coexisting high-and low-calcium melts identified by mineral and melt inclusion studies of a subduction-influenced syn-collisional magma from South Sulawesi, Indonesia. Journal of Petrology, 47 (12), 2433-2462.

Harmon, R.S., and Hoefs, J. (1995) Oxygen isotope heterogeneity of the mantle deduced from global ^{18}O systematic of basalts from different geotectonic settings. Contributions to Mineralogy and Petrology, 120 (1), 95-114.

Hart, S.R., and Davis, K.E. (1978) Nickel partitioning between olivine and silicate melt. Earth and Planetary Science Letters, 40, 203-219.

Hesse, M., and Grove, T.L. (2003) Absarokites from the Western Mexican Volcanic Belt: constraints on mantle wedge conditions. Contributions to Mineralogy and Petrology, 146, 10-27.

Ishimaru, S., and Arai, S. (2008) Nickel enrichment in mantle olivine beneath a volcanic front. Contributions to Mineralogy and Petrology, 156, 119-131.

Johnson E.R., Wallace, P.J., Delgado Granados, H., Manea, V.C., Kent, A.J.R., Bindeman, I.N.,

and Donegan C. (2009) Subduction-related volatile recycling and magma generation beneath Central Mexico: insights from melt inclusions, oxygen isotopes and geodynamic models. Journal of Petrology, 50 (9), 1729-1764.

Jugo, P.J., Wilke, M., and Botcharnikov, R.E. (2010) Sulfur K-edge XANES analysis of natural and synthetic basaltic glasses: Implications for S speciation and S content as a function of oxygen fugacity. Geochimica et Cosmochimica Acta, 74, 5926-5938.

Jurewicz, A.J.G., and Watson, E.B. (1988) Cations in olivine, Part I: calcium partitioning and calcium-magnesium distribution between olivine and coexisting melts, with petrologic applications. Contributions to Mineralogy and Petrology, 99, 176-185.

Kamenetsky, V.S., Sobolev, A.V., Joron, J.-L., and Semet, P. (1995) Petrology and geochemistry of Cretaceous ultramafic volcanics from eastern Kamchatka. Journal of Petrology, 36 (3), 637-662.

Kamenetsky, V.S., Crawford, A.J. and Meffre, S. (2001) Factors controlling chemistry of magmatic spinel: an empirical study of associated olivine, Cr-spinel and melt inclusions from primitive rocks. Journal of Petrology, 42, 655-671.

Kamenetsky, V.S., Elburg, M., Arculus, R., and Thomas, R. (2006) Magmatic origin of low-Ca olivine in subduction-related magmas: Co-existence of contrasting magmas. Chemical Geology, 233, 346-357.

Kamenetsky, V.S., Kamenetsky, M.B., Sobolev, A.V., Golovin, A.V., Demouchy, S., Faure, K., Sharygin, V.V., and Kuzmin, D.V. (2008). Olivine in the Udachnaya-East Kimberlite (Yakutia, Russia): types, compositions and origins. Journal of Petrology, 49 (4), 823-839.

Kay, R.W. (1978) Aleutian magnesian andesites: Melts from subducted Pacific Ocean crust. Journal of Volcanology and Geothermal Research, 4, 117-132.

Kinzler, R.J., Grove, T.L., and Recca, S.I. (1990) An experimental study on the effect of temperature and melt composition on the partitioning of nickel between olivine and silicate melt. Geochimica et Cosmochimica Acta, 54, 1255-1265.

Leeman, W.P., and Scheidegger, K.F. (1977) Olivine/liquid distribution coefficients and a test for crystal-liquid equilibrium. Earth and Planetary Science Letters, 35, 247-257.

Leeman, W.P., and Lindstrom, D.J. (1978) Partitioning of Ni2+ between basaltic and synthetic melts and olivine- an experimental study. Geochimica et Cosmochimica Acta, 42, 801-816.

Leeman, W.P., Lewis, J.F., Evarts, R.C., Conrey, R.M., and Streck, M.J. (2005) Petrologic constraints on the thermal structure of the Cascades arc. Journal of Volcanology and Geothermal Research, 140, 67-105.

Li, C., and Ripley, E.M. (2010) The relative effects of composition and temperature on olivine-

732 liquid Ni partitioning: Statistical deconvolution and implications for petrologic modeling.
733 Chemical Geology, 274, 99-104.
734
735 Libourel, G. (1999) Systematics of calcium partitioning between olivine and silicate melt:
736 implications for melt structure and calcium content of magmatic olivine. Contributions to
737 Mineralogy and Petrology, 136, 63-80.
738
739 Luhr, J.F. (1997) Extensional tectonics and the diverse primitive volcanic rocks in the western
740 Mexican volcanic belt. The Canadian Mineralogist, 35 Part 2, 473-500.
741
742 Mattey, D. P., Lowry, D., and Macpherson, C. (1994) Oxygen isotope composition of mantle
743 peridotite. Earth and Planetary Science Letters, 128, 231-241.
744
745 McDonough, W.F., and Sun, S.S. (1995) The composition of the Earth. Chemical Geology, 120,
746 223-253.
747
748 Metrich, N., Berry, A.J., O'Neill, H. St.C., and Susini, J. (2009) The oxidation state of sulfur in
749 synthetic and natural glasses determined by X-ray absorption spectroscopy. Geochimica et
750 Cosmochimica Acta, 73, 2382-2399.
751
752 Muan, A., and Osborne, E. (1956) Phase equilibria at liquidus temperatures in the system MgO-
753 FeO-Fe2O3-SiO2. Journal of the American Ceramic Society, 39, 121-140.
754

Muehlenbachs, K. (1986) Alteration of the oceanic crust and the ^{18}O history of seawater. Stable isotopes in high temperature geological processes. Valley, John W., Taylor, Hugh P., Jr., O'Neil, James R. (eds). Reviews in Mineralogy, 16, 425-444.

Pilbeam, L.H., Nielsen, T.F.D., and Waight, T.E. (2013) Digestion fractional crystallization (DFC): an important process in the genesis of kimberlites. Evidence from olivine in the Majuagaa Kimberlite, Southern West Greenland. Journal of Petrology, 54 (7), 1399-1425.

Reiners, P.W., Hammond, P.E., McKenna, J.M., and Duncan, R.A. (2000) Young basalts of the central Washington Cascades, flux melting of the mantle, and trace element signatures of primary arc magmas. Contributions to Mineralogy and Petrology, 138, 249-264.

Roedder, E., and Emslie, R. (1970) Olivine-liquid equilibrium. Contributions to Mineralogy and Petrology, 29, 275-289.

Rowe, M.C., Nielsen, R.L., and Kent, A.J.R. (2006) Anomalously high Fe contents in rehomogenized olivine hosted melt inclusions from oxidized magmas. American Mineralogist, 91, 82-91.

Rowe, M.C., Kent, A.J.R., and Nielsen, R.L. (2007) Determination of sulfur speciation and oxidation state of olivine hosted melt inclusions. Chemical Geology, 236, 303-322.

Rowe, M.C., Nielsen, R.L., and Kent, A.J.R. (2009) Subduction influence on oxygen fugacity

778 and trace and volatile elements in basalts across the Cascade volcanic arc. Journal of Petrology,
779 50 (1), 61-91.
780
781 Sack, R., Carmichael, I., Rivers, M., and Ghiorso, M. (1980). Ferric-ferrous equilibria in natural
782 silicate liquids at 1 bar. Contributions to Mineralogy and Petrology, 75, 369-376.
783
784 Schmidt, M.E., Grunder, A.L., and Rowe, M.C. (2008) Segmentation of the Cascade arc as
785 indicated by Sr and Nd isotopic variation among diverse primitive basalts. Earth and Planetary
786 Science Letters, 266, 166-181.
787
788 Schmidt, M.E., Grunder, A.L., Rowe, M.C., and Chesley, J.T. (2013) Re and Os isotopes of the
789 central Oregon Cascades and along the arc indicate variable homogenization and mafic growth in
790 the deep crust. Geochimica et Cosmochimica Acta, 109, 345-364.
791
792 Simkin, T., and Smith, J.V. (1970) Minor-element distribution in olivine. Journal of Geology, 78,
793 304-325.
794
795 Sobolev, A.V., Hofmann, A.W., Sobolev, S.V., and Nikogosian, I.K. (2005) An olivine-free
796 mantle source of Hawaiian shield basalts. Nature, 434, 590-597.
797
798 Sobolev, A.V., Hofmann, A.W., Kuzmin, D.V., Yaxley, G.M., Arndt, N.T., Chung, S-L.,
799 Danyushevksy, L.V., Elliott, T., Frey, F.A., Garcia, M.O., and others (2007) The amount of
800 recycled crust in sources of mantle-derived melts. Science, 316, 412-417.

Stein, S., and Stein, C. (1996) Thermo-mechanical evolution of oceanic lithosphere: implications for the subduction process and deep earthquakes. In: G. Bebout, D. Scholl, S. Kirby, and J. Platt (Eds.). Subduction Top to Bottom. American Geophysical Union Monograph 96, 1-18.

Stormer, J.C., Jr. (1973) Calcium zoning in olivine and its relationship to silica activity and pressure. Geochimica et Cosmochimica Acta, 37 (8), 1815-1821.

Straub, S.M., LaGatta, A.B., Pozzo, A.L., and Langmuir, C.H. (2008) Evidence from high-Ni olivine for a hybridized peridotite/pyroxenite source for orogenic andesites from the central Mexican Volcanic Belt. Geochemistry, Geophysics, Geosystems, 9, doi: 10.1029/2007GC001583.

Straub, S.M., Gomez-Tuena, A., Stuart, F.M., Zellmer, G.F., Espinasa-Perena, R., Cai, Y., and Iizuka, Y. (2011) Formation of hybrid arc andesites beneath thick continental crust. Earth and Planetary Science Letters, 303, 337-347.

Straub, S.M., Zellmer, G.F., Gomez-Tuena, A., Espinasa-Perena, R., Martin-Del Pozzo, A.L., Stuart, F.M., and Langmuir C.H. (2014) A genetic link between silicic slab components and calc-alkaline arc volcanism in central Mexico. In A. Gomez-Tuena, S.M. Straub, and G.F. Zellmer, (eds) Orogenic Andesites and Crustal Growth, Geological Society, London, Special Publications, 385, 31-64.

Syracuse, E.M., van Keken, P.E., and Abers, G.A. (2010) The global range of subduction zone thermal models. Physics of the Earth and Planetary Interiors, 183, 73-90.

Tatsumi, Y., Suzuki, T., Kawabata, H., Sato, K., Miyazaki, T., Chang, Q., Takahashi, T., Tani, K., Shibata, T., and Yoshikawa, M. (2006) The petrology and geochemistry of Oto-Zan composite lava flow on Shodo-Shima Island, SW Japan: Remelting of a solidified high-Mg andesite magma. Journal of Petrology 47, (3) 595-629.

Wallace, P.J., and Carmichael, I.S.E. (1994) S speciation in submarine basaltic glasses as determined by measurements of SKα X-ray wavelength shifts. American Mineralogist, 79, 161-167.

Wang, Z., and Gaetani, G.A. (2008) Partitioning of Ni between olivine and siliceous eclogite partial melt: experimental constraints on the mantle source of Hawaiian basalts. Contributions to Mineralogy and Petrology, 156, 661-678.

Figure Captions

Figure 1. Location map for the Quartzville basalt within the Oregon Cascades. The older Western Cascades (dark grey; ~ 40-10 Ma) are distinguished from the younger High Cascades (light grey; ~10 Ma – present). Major volcanic centers in the High Cascades are indicated with triangles. The position of the Quartzville basalt (QV; 42 ka) is indicated within the older Western

847 Cascades.

848

849 **Figure 2**. Olivine thin section petrographic images indicating the range of textures and
850 morphologies observed. Predominantly euhedral grains (a; c) are most common, however,
851 skeletal or partial grains are sometimes observed (b). Magnetite and/or spinel inclusions in
852 olivine may be zoned (a), or randomly distributed. Chains of oxide phases (+/- a silicate phase),
853 increase in size into the grain, perpendicular to grain boundary (c, d).

854

855 **Figure 3**. X-ray mapping of Mg (a, c), Mn (b), and Ni (d), variations in an olivine grain from the
856 lava flow. Note that Mg intensity increases (indicated by warm colors) around the olivine rim,
857 characteristic of the high-Fo rim compositions. Additionally, Mn X-ray intensities increase
858 towards the rim while Ni decreases, consistent with quantitative transect measurements.

859

860 **Figure 4**. Representative backscatter electron images (BSE) of clinopyroxene sector (a) and
861 oscillatory (b) zonation and textures and corresponding calculated Fe_2O_3/FeO along analytical
862 transects (c, d). Oscillatory zoning is evident in some grains (b), with grain rims having high Fe
863 concentrations.

864

865 **Figure 5**. Backscatter electron image (BSE) of the scoria glass in contact with an olivine
866 phenocryst. Groundmass is dominated by clinopyroxene and olivine with microapatite. Olivine
867 compositions are indicated for the phenocryst and groundmass grains.

868

869 **Figure 6**. (a) Ni and (b) Ca concentrations (ppm) versus olivine Fo# for Quartzville olivine

grains from both the scoria (open) and lava (closed).

Figure 7. Ca versus Ni variations in olivine. (a) Quartzville Ca and Ni olivine concentrations overlain on a 2D smoothed histogram of a compilation of mantle olivine (Fo89-93; N= 4444) from the georoc database (http://georem.mpch-mainz.gwdg.de/). Also indicated are the starting (green square) and ending (red star) compositions assuming Ni and Ca partitioning and olivine fractionation (from Fo_{91} to Fo_{89}) as described in the text. The black line is a linear regression of olivine chemical variation based on olivine with less than 4500 ppm Ni, showing the offset at higher Ni concentrations. (b) Normalized Ca and Ni variations after Sobolev et al. (2007), compared to olivine compositions from other Cascade arc end-member magmas which generally are higher Ca and lower Ni (data from Rowe et al., 2009). Also plotted (dashed ellipses) are the fields olivine derived from pyroxenite and peridotite sources from Sobolev et al. (2007). Same symbols as in figure 6.

Figure 8. Representative core-rim transects across olivine grains from the lava (a-d) and scoria (e-h) for Fo# (a, e), Ni (b, f), Ca (c, g), and Mn (d, h).

Figure 9. Oxygen isotope ($\delta^{18}O$) variation of olivine phenocrysts from Cascades basalts, versus whole rock MgO wt. %. Upper mantle olivine field from Mattey et al. (1994). Quartzville is indicated as the black square. Arc lavas and backarc lavas (shoshonite, calc-alkaline basalts, enriched intraplate basalt, and low-K tholeiites) are classified after Rowe et al. (2009).

Figure 10. Lava, scoria and melt inclusion trace element compositions normalized to primitive

mantle (McDonough and Sun, 1995). Note significant heavy rare earth element depletion and consistency between lava, scoria, and average melt inclusions. Modified from Rowe et al. (2006, 2009).

Figure 11. Schematic model of mantle processes in the generation of the Quartzville basalt. Depth of ecologitized crust from Bostock et al. (2002). (1) Slab partial melting of ecolgitic crust resulting in a siliceous melt with an adakite-like trace signature (e.g., high Sr/Y, La/Yb). Box shows enlargement of proposed re-equilibration model where the high-SiO_2 melt reacts with the olivine in the depleted harzburgite to generate reaction-pyroxenite (red). Trace element re-equilibration extends (grey) beyond the silica + olivine = orthopyroxene reaction such that melting of both zones will have a similar trace element signature. High Ni, low Ca olivine crystallizes from a melt of reaction-pyroxenite, while lower Ni, high Ca olivine rims crystalize from melt derived from slab fluid-fluxed depleted harzburgite at (2).

Table 1. Summary of the petrography for scoria and lava, and olivine compositional details.

	Phases	*Characteristics*	*Compositions*	*Transect details*
			Scoria	
Phenocrysts	olivine	euhedral, up to 500 μm; no magnetite inclusions in olivine	$Fo_{90.6\text{-}88.4}$ Ni 1100-5500 ppm Ca 658-1746 ppm Mn 730-1617 ppm	normally zoned rim compositions $Fo_{88.7\text{-}89.4}$ Ni decreases from 5000-6000 ppm in cores to 1000-2000 ppm in rims Ca varies inversely with Ni
Groundmass	olivine > clinopyroxene > apatite		Fo_{89} Ni 1310-1860 ppm Ca 1605-1940 ppm	
			Lava	
Phenocrysts	olivine	euhedral-subhedral, some broken, some embayed edges, up to 500 μm abundant magnetite-spinel inclusions	$Fo_{93.8\text{-}88.6}$, Ave. $Fo_{90.7}$ Ni 800-6400 ppm Ca 860-1785 ppm Mn 680-2320 ppm	both normal (predominant; rim composition ~Fo_{89}) and reverse (minor; only in outer 50 μm; up to ~Fo_{94}) zoning Ni does not vary linearly with Fo content; Max Ni at ~Fo_{91}; Ni decreases to higher and lower Ca varies inversely with Ni Mn varies inversely with Ni
	clinopyroxene microphenocrysts	euhedral, up to 400 μm, most <200 μm	Mg# 82-89	increase in Fe_2O_3/FeO toward rim
Groundmass	Plagioclase-clinopyroxene > magnetite > apatite	decreasing S at rims of apatite	Cpx Mg# ~86	

Table 2: Representative and average olivine compositions from the lava and scoria samples.

Oxide (wt%)	SiO_2	Al_2O_3	MnO	FeO	NiO	MgO	CaO	TiO_2	Cr_2O_3	Total	Fo#
Scoria											
Average	40.17	0.03	0.14	10.24	0.40	48.49	0.17	0.01	0.04	99.68	89.4
s.d.	0.56	0.05	0.03	0.63	0.13	0.49	0.03	0.01	0.02	0.58	0.6
04-053-5.1	40.37	0.02	0.14	11.00	0.22	48.51	0.24	0.00	0.03	100.54	88.7
04-036_4.12	40.76	0.01	0.12	10.09	0.42	48.40	0.15	0.01	0.06	100.02	89.5
04-036_1.1	40.90	0.01	0.13	9.25	0.64	48.80	0.13	0.01	0.08	99.96	90.4
g.m. rim	40.47	0.04	0.17	10.59	0.14	47.49	0.28	0.04	0.02	99.26	88.9
g.m. core	40.24	0.05	0.18	10.32	0.26	47.76	0.23	0.01	0.04	99.10	89.2
Lava											
Average	40.42	0.03	0.13	8.97	0.55	49.06	0.15	0.01	0.05	99.37	90.7
s.d.	0.34	0.07	0.04	0.84	0.14	0.82	0.04	0.01	0.03	0.57	0.9
04-044-5.1	39.54	0.00	0.14	10.79	0.31	48.35	0.16	0.01	0.01	99.30	88.9
03-050-7.1	40.14	0.03	0.12	9.53	0.51	48.36	0.13	0.00	0.03	98.85	90.0
04-047-22.1	40.40	0.01	0.09	8.62	0.76	48.76	0.12	0.00	0.07	98.83	91.0
03-1_1.1	40.81	0.02	0.17	7.65	0.49	49.89	0.14	0.01	0.03	99.25	92.1
03-1_3.26	41.01	0.00	0.30	6.06	0.10	51.64	0.23	0.02	0.02	99.39	93.8

Note: "g.m." denotes groundmass olivine.

Ni, ppm	Ca, ppm	Mn, ppm
3011	1212	1091
949	242	206
1723	1723	1107
3306	1107	896
5003	926	1025
1093	1995	1280
2031	1612	1399
4284	1038	992
1065	268	274
2431	1126	1056
4031	933	918
5963	861	681
3879	1015	1322
789	1647	2320

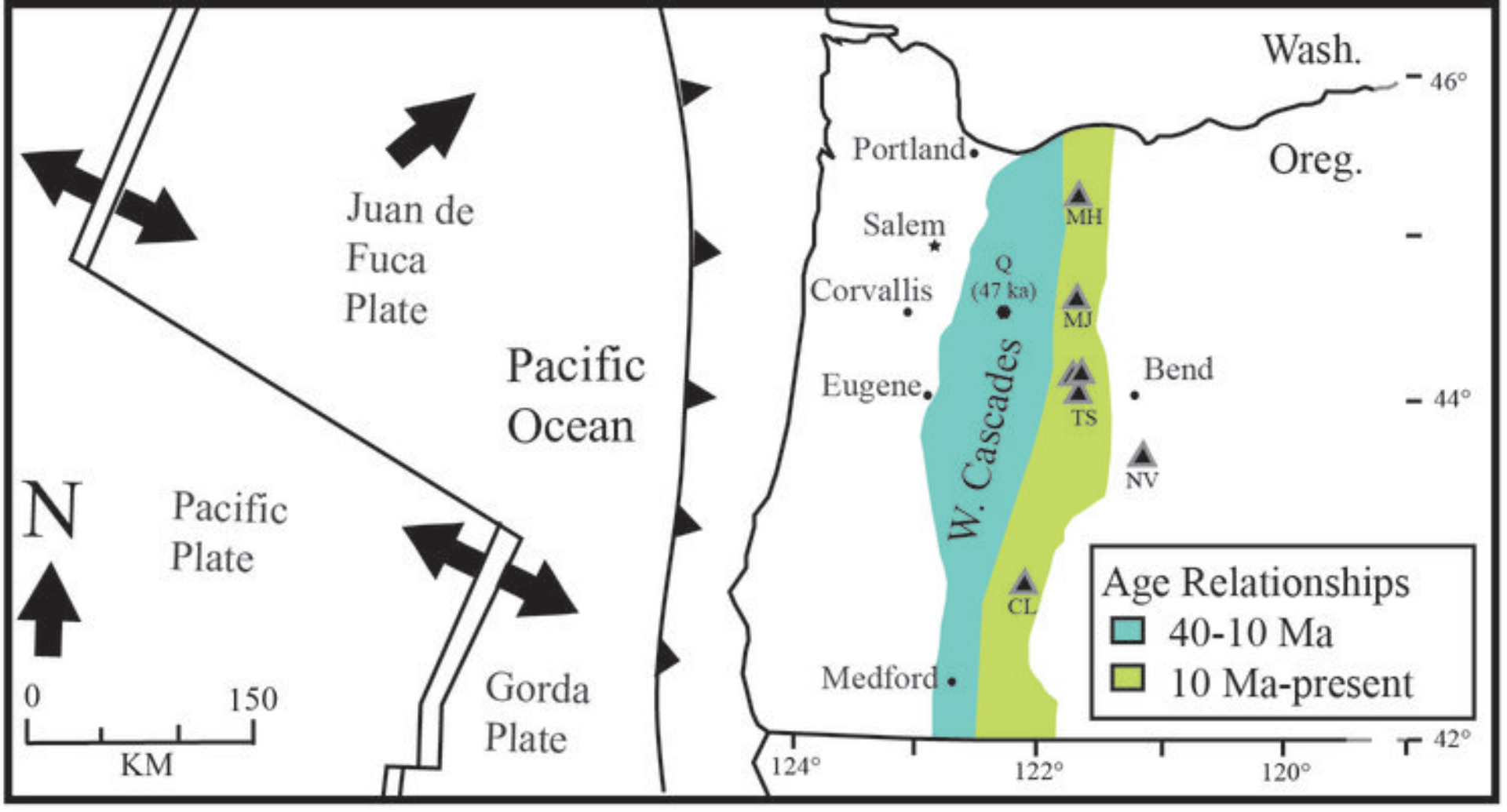
Juan de
Fuca
Plate
Pacific
Ocean
N
Pacific
Plate
Gorda
Plate
0
150
KM
Wash.
46°
Portland
Oreg.
Salem
Corvallis
Q
(47 ka)
MH
MJ
Eugene
Bend
TS
NV
W. Cascades
CL
Medford
44°
42°
124°
122°
120°
Age Relationships
40-10 Ma
10 Ma-present

Figure 1

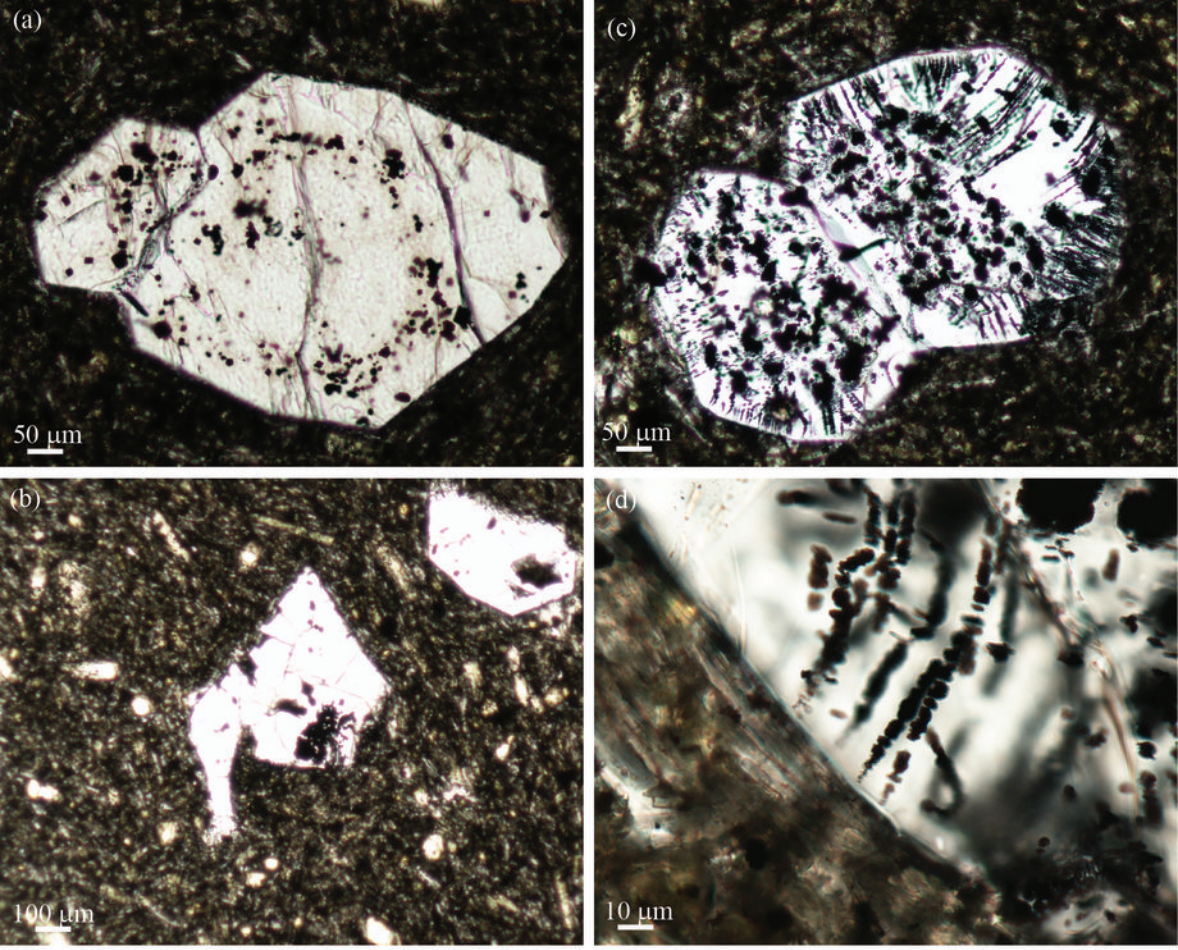

Figure 2

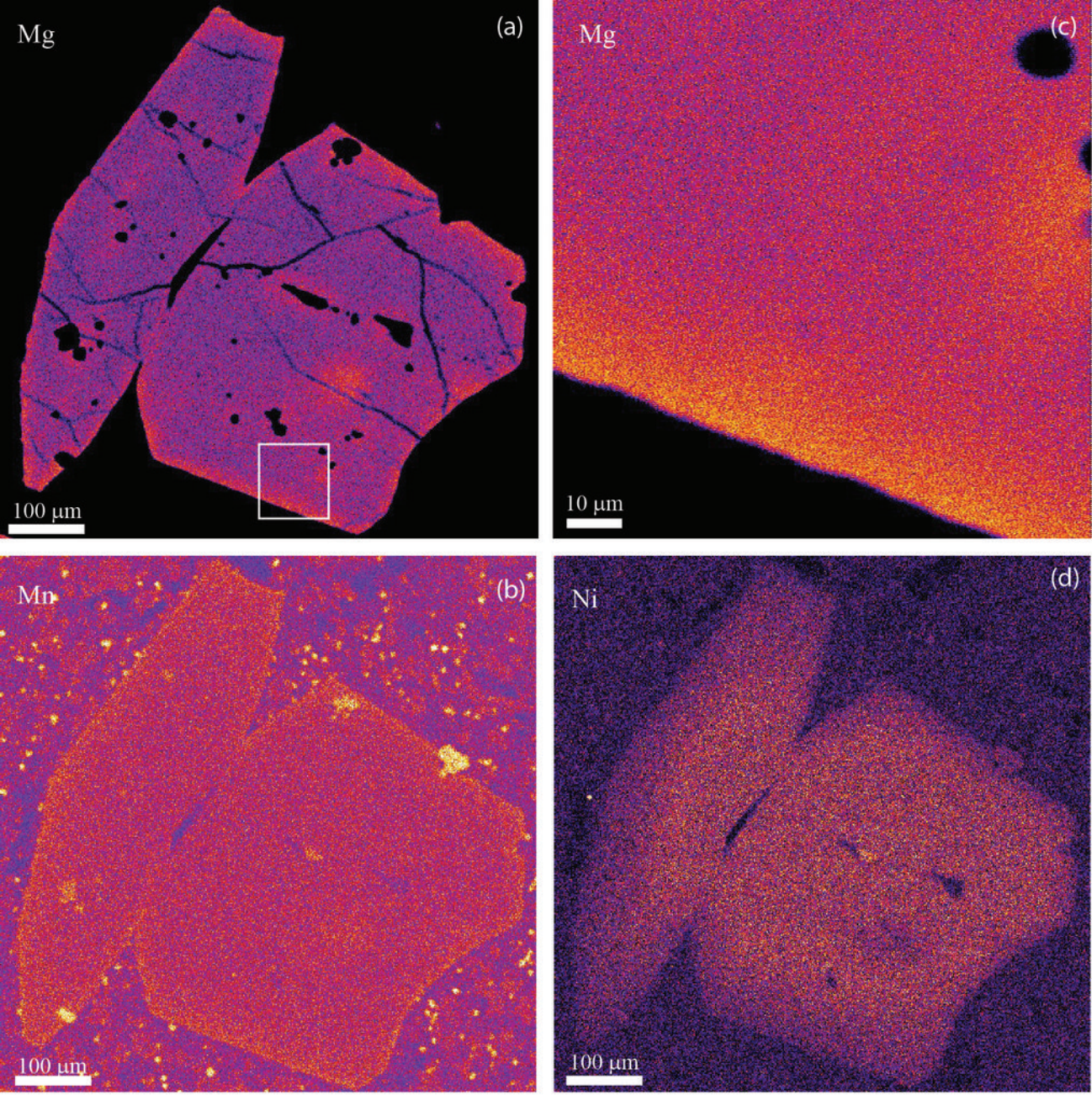

Figure 3

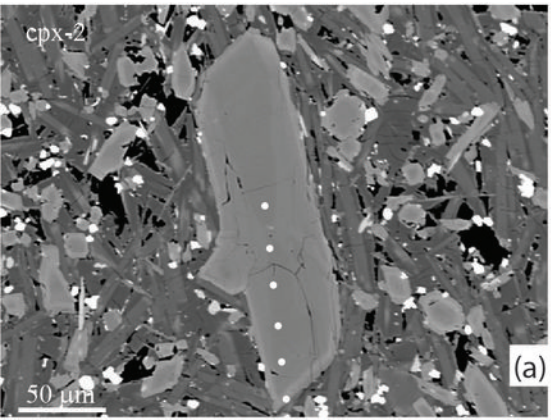
cpx-2
50 μm
(a)

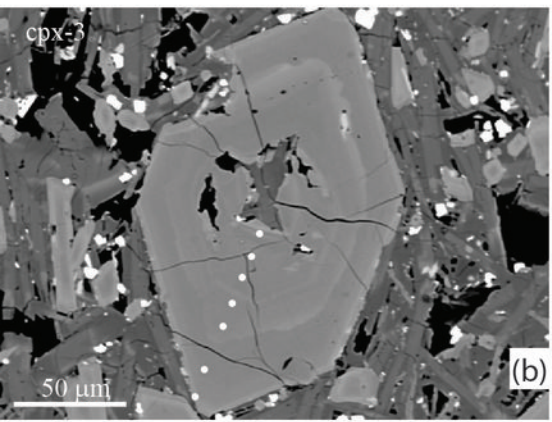
cpx-3
50 μm
(b)

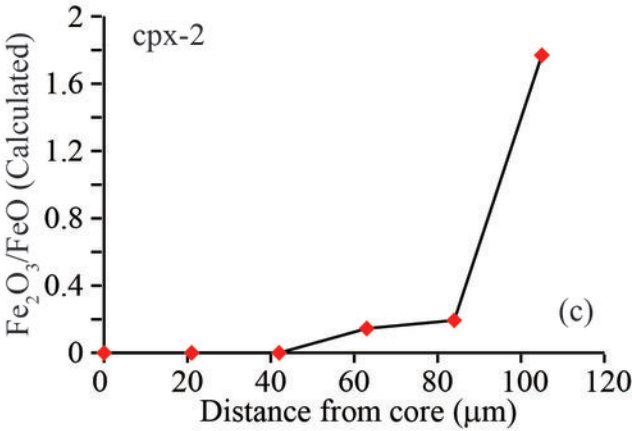
cpx-2
Fe2O3/FeO (Calculated)
0
0.4
0.8
1.2
1.6
2
0
20
40
60
80
100
120
Distance from core (μm)
(c)

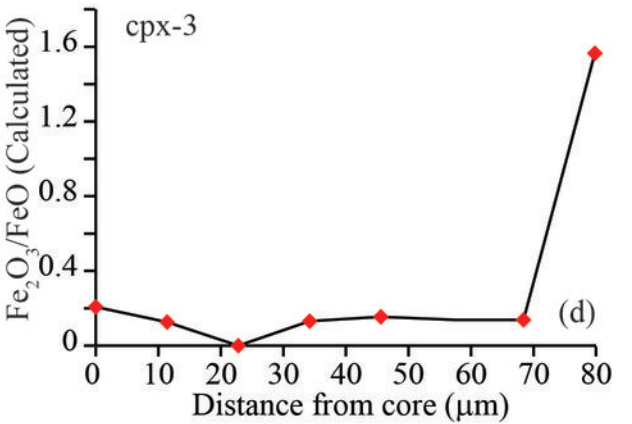
cpx-3
Fe2O3/FeO (Calculated)
0
0.4
0.8
1.2
1.6
0
10
20
30
40
50
60
70
80
Distance from core (μm)
(d)

Figure 4

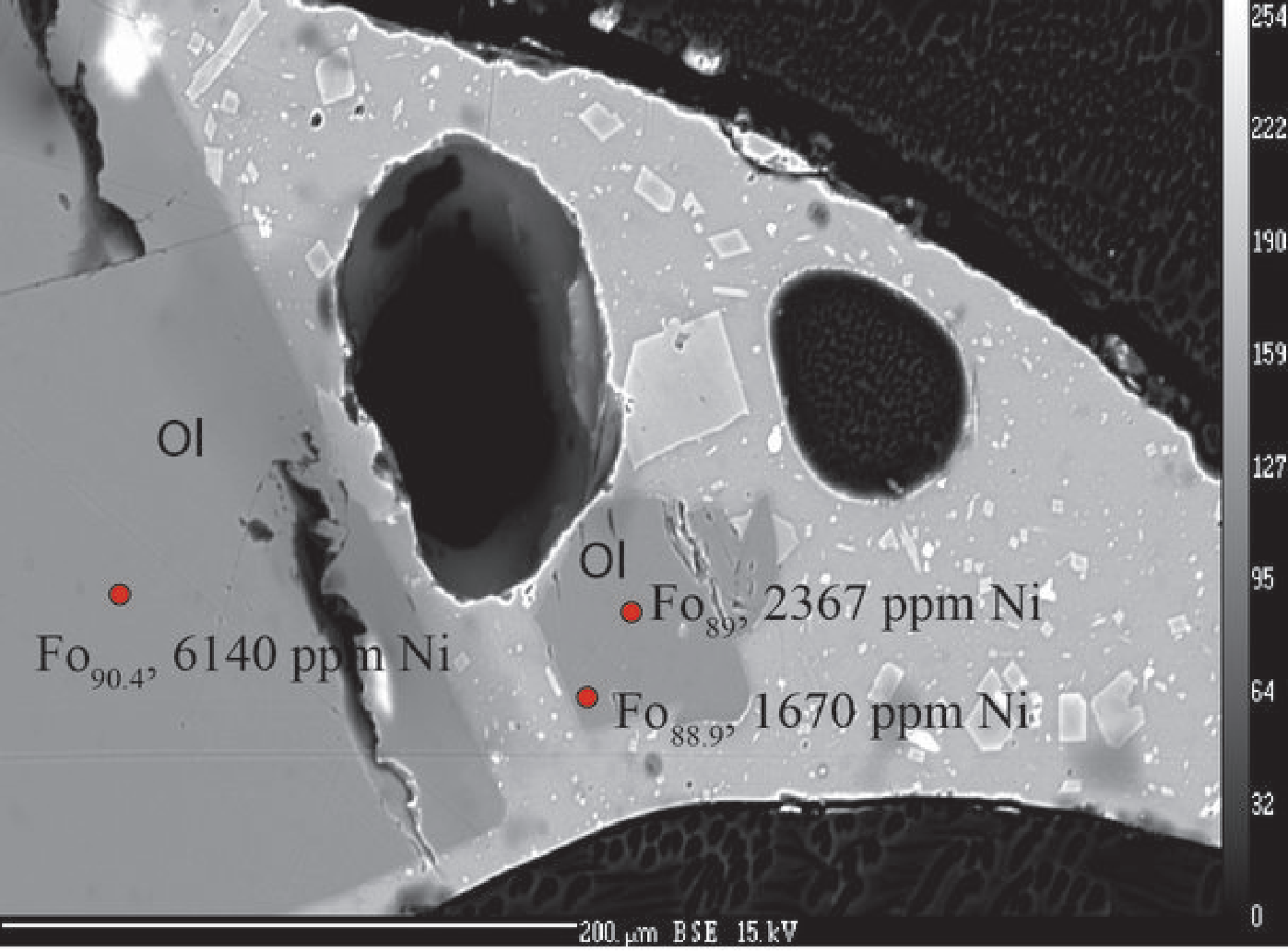
Ol
Ol
Fo90.4, 6140 ppm Ni
Fo89, 2367 ppm Ni
Fo88.9, 1670 ppm Ni
200 µm BSE 15 kV
254
222
190
159
127
95
64
32
0

Figure 5

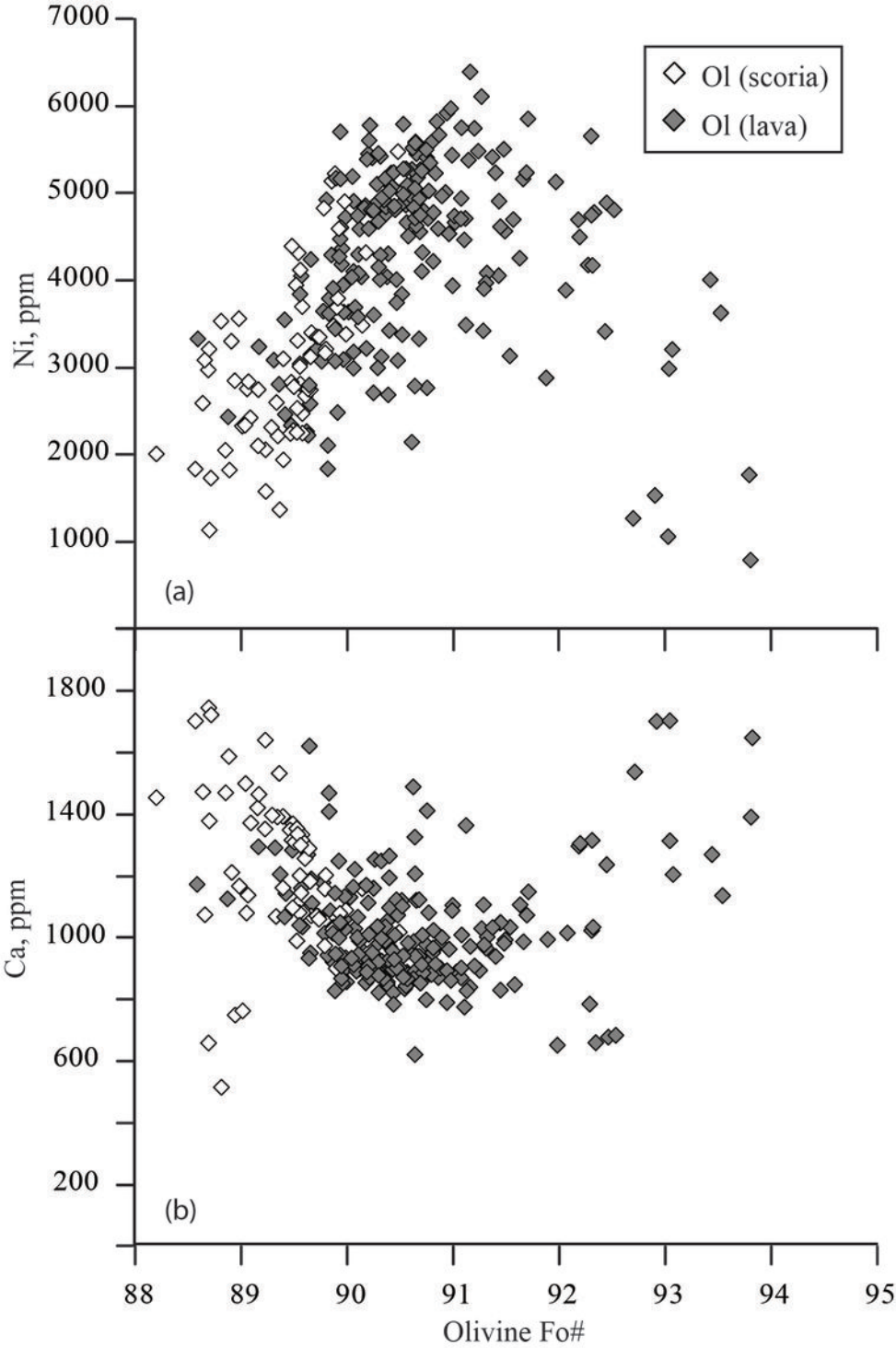
Ol (scoria)
Ol (lava)
Ni, ppm
7000
6000
5000
4000
3000
2000
1000
(a)
Ca, ppm
1800
1400
1000
600
200
(b)
88
89
90
91
92
93
94
95
Olivine Fo#

Figure 6

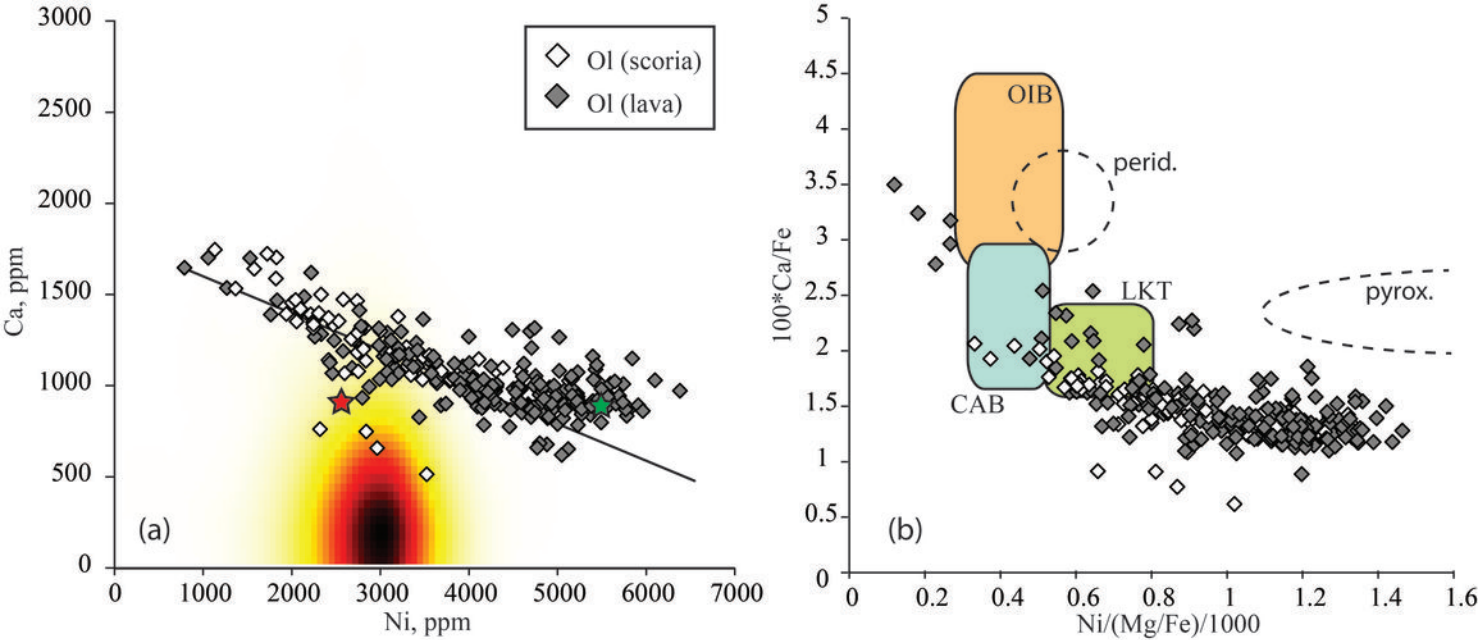
Ol (scoria)
Ol (lava)
Ca, ppm
Ni, ppm
(a)
OIB
perid.
LKT
pyrox.
CAB
100*Ca/Fe
Ni/(Mg/Fe)/1000
(b)

Figure 7

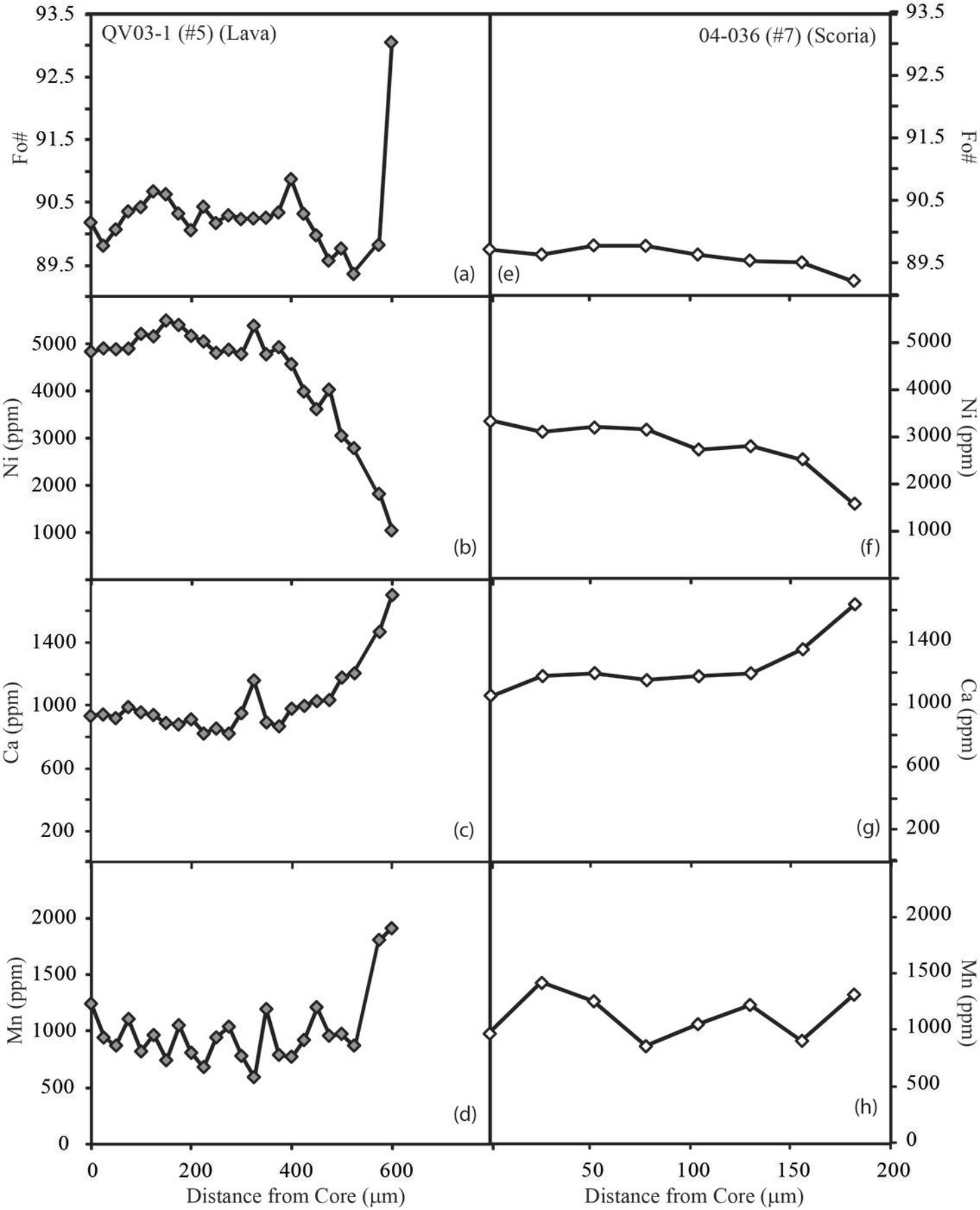
QV03-1 (#5) (Lava)
04-036 (#7) (Scoria)
Fo#
Ni (ppm)
Ca (ppm)
Mn (ppm)
(a)
(b)
(c)
(d)
(e)
(f)
(g)
(h)
Distance from Core (μm)
Distance from Core (μm)

Figure 8

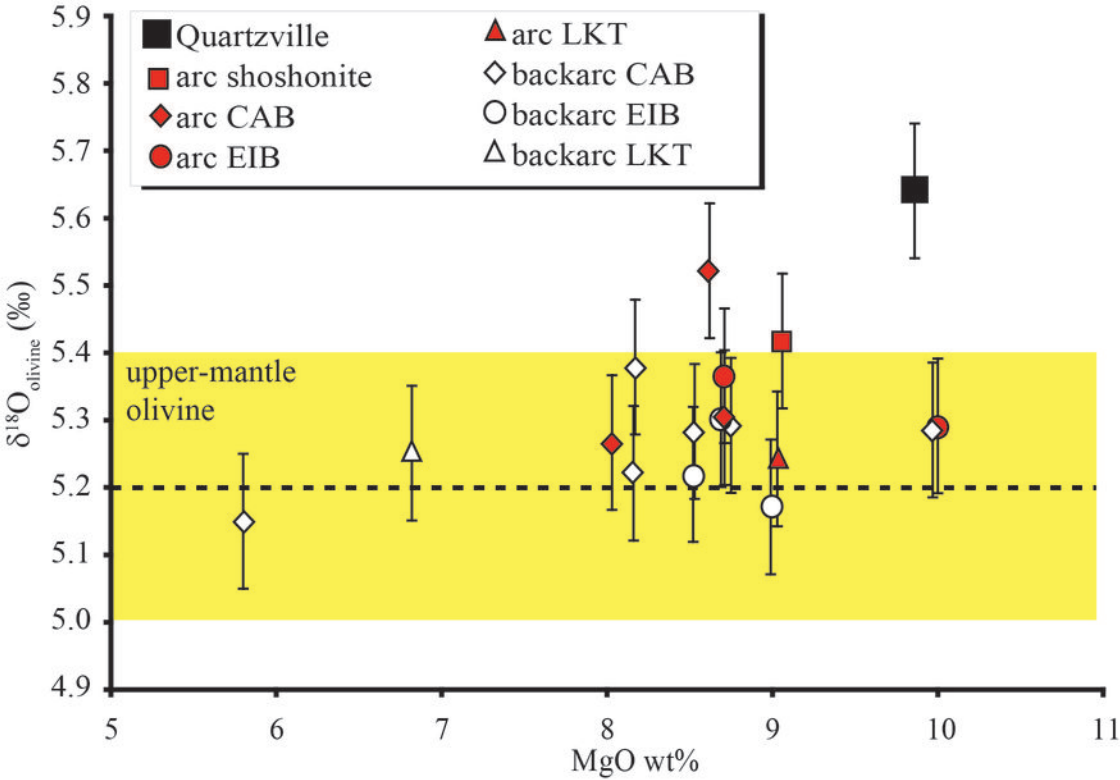
Quartzville
arc shoshonite
arc CAB
arc EIB
arc LKT
backarc CAB
backarc EIB
backarc LKT
upper-mantle olivine
δ18Oolivine (‰)
MgO wt%
5.9
5.8
5.7
5.6
5.5
5.4
5.3
5.2
5.1
5.0
4.9
5
6
7
8
9
10
11

Figure 9

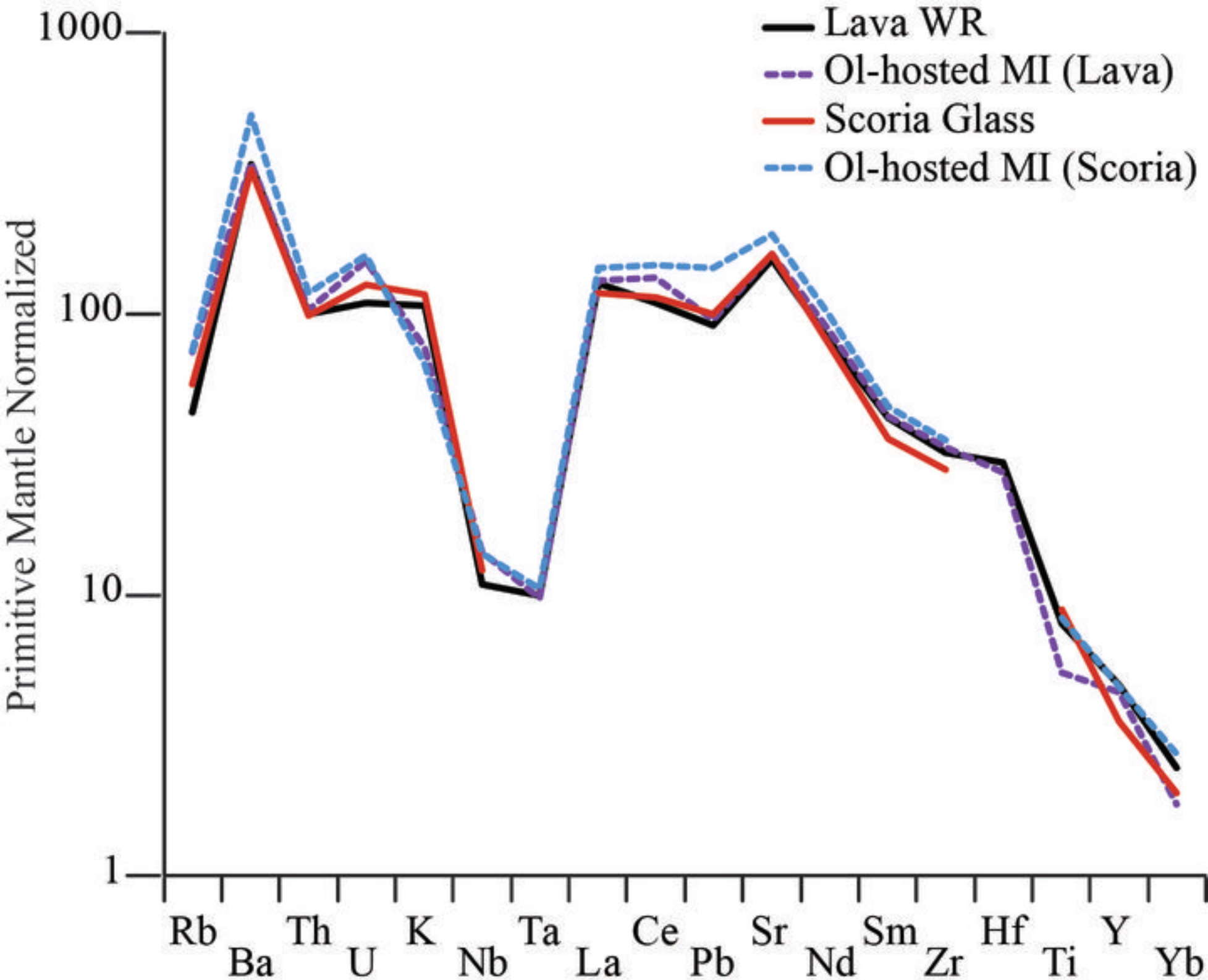
Lava WR
Ol-hosted MI (Lava)
Scoria Glass
Ol-hosted MI (Scoria)
Primitive Mantle Normalized
1000
100
10
1
Rb
Ba
Th
U
K
Nb
Ta
La
Ce
Pb
Sr
Nd
Sm
Zr
Hf
Ti
Y
Yb

Figure 10

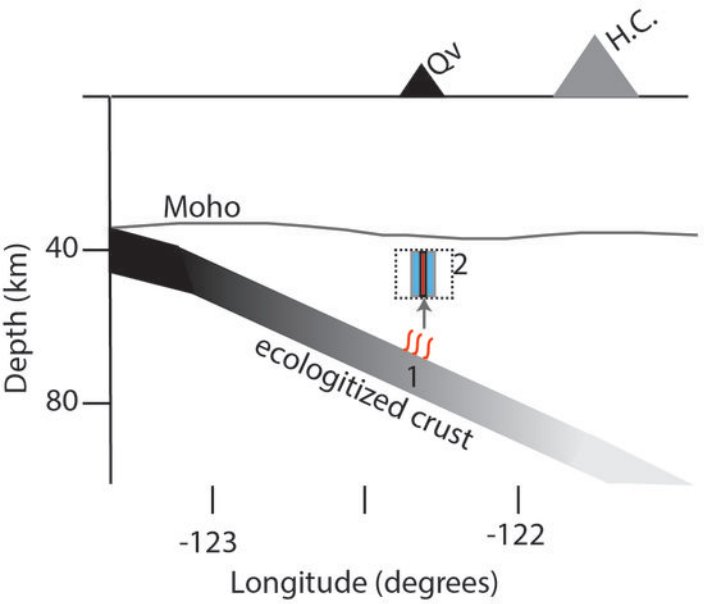
Qv
H.C.
Moho
40
80
Depth (km)
2
1
ecologitized crust
-123
-122
Longitude (degrees)

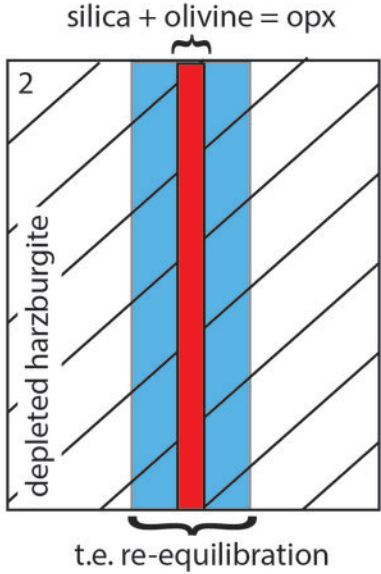
silica + olivine = opx
2
depleted harzburgite
t.e. re-equilibration

Figure 11